Yuxuan Cai

Condition monitoring and fault detection for marine battery energy storage system

Master's thesis in Marine Technology
Supervisor: Roger Skjetne
Co-supervisor: Namireddy Praveen Reddy, Zhengru Ren
June 2021

Master's thesis

NTNU

Norwegian University of
Science and Technology

Yuxuan Cai

Condition monitoring and fault detection for marine battery energy storage system

Master's thesis in Marine Technology
Supervisor: Roger Skjetne
Co-supervisor: Namireddy Praveen Reddy, Zhengru Ren
June 2021

Norwegian University of Science and Technology
Faculty of Engineering
Department of Marine Technology

NTNU
Norwegian University of
Science and Technology

MASTER OF TECHNOLOGY THESIS DEFINITION (30 SP)

Name of the candidate:	Cai, Yuxuan
Field of study:	Marine cybernetics
Thesis title (Norwegian):	Tilstandsovervåkning og feilprediksjon for marine batterisystemer
Thesis title (English):	Condition monitoring and failure prediction for marine battery energy storage systems

Background

During the last decade, enabling technologies in energy storage, especially battery-based systems, have resulted in new hybrid-electric and pure battery-electric power and propulsion solutions to reduce fuel consumption and emissions in ships. Mixing diesel-generators and battery energy storage systems (BESS) in a hybrid power system enables various control strategies, such as power smoothing, peak-shaving, strategic loading, start-stop operation of the diesel genset, etc.

In order to use the battery in a safe and optimal manner, exact information of stored energy (charges), health (or ageing), discharge and charge rates (c-rate and maximum power), failure symptoms, etc., are necessary to be estimated and monitored. Furthermore, failures must rapidly be detected and those imminent to happen should be predicted.

The main objective of this project is to study state-of-the-art BESS solutions related to battery condition monitoring, involving relevant states and state-estimation methods for the important BESS parameters, including failure prediction and detection. Of particular interest is to study machine learning methods and compare these to more traditional Kalman filtering (KF) methods on equivalent circuit models. In the project, relevant datasets should be found or synthesized, methods implemented for the prediction, detection, and estimation problems, and results (with comparing/contrasting) to be analyzed and discussed.

Scope of Work

1) Perform a background and literature review to provide information and relevant references on:
   - Marine battery storage solutions, incl. parts, control functions, and auxiliaries.
   - Battery parameters and related models for condition monitoring and control, in particular methods/algorithms for SoC/SoH estimation and failure prediction/detection.
   - Relevant physics-based (model-based) and data-driven methods (machine learning methods) for the estimation, prediction, and detection problems.
   - Relevant datasets, if this can be found.

   Write a list with abbreviations and definitions of terms and symbols, relevant to the literature study and project report.

2) Implement and test estimation methods, comparing data-driven methods with ECM-based estimation, particularly KF-based methods, considering:

   a) SoC estimation,

   b) maximum power estimation, and

   c) SoH estimation.

   Analyze and discuss the resulting performance of each problem and method.

3) Present and discuss the common failures that may occur in BESS, being important to predict and detect. What data is necessary to identify these failures? What models are relevant?

4) Propose, implement, and test relevant method(s) related to failure prediction and detection for BESS. Analyze and discuss the resulting performance.

Specifications

<u>Every weekend throughout the project period, the candidate shall send a status email to the supervisor and co-advisors, providing two brief bulleted lists: 1) work done recent week, and 2) work planned to be done next week.</u>

The scope of work may prove to be larger than initially anticipated. By the approval from the supervisor, described topics may be deleted or reduced in extent without consequences with regard to grading.

The candidate shall present personal contribution to the resolution of problems within the scope of work. Theories and conclusions should be based on mathematical derivations and logic reasoning identifying the steps in the deduction.

The report shall be organized in a logical structure to give a clear exposition of background, problem/research statement, design/method, analysis, and results. The text should be brief and to the point, with a clear language. Rigorous mathematical deductions and illustrating figures are preferred over lengthy textual descriptions. The report shall have font size 11 pts., and it is not expected to be longer than 70 A4-pages, 100 B5-pages, from introduction to conclusion, unless otherwise agreed. It shall be written in English (preferably US) and contain the elements: Title page, abstract, preface (incl. description of help, resources, and internal and external factors that have affected the project process), acknowledgement, project definition, list of symbols and acronyms, table of contents, introduction (project background/motivation, objectives, scope and delimitations, and contributions), technical background and literature review, problem formulation, method, results and analysis, conclusions with recommendations for further work, references, and optional appendices. Figures, tables, and equations shall be numerated. The original contribution of the candidate and material taken from other sources shall be clearly identified. Work from other sources shall be properly acknowledged using quotations and a Harvard citation style (e.g. natbib Latex package). The work is expected to be conducted in an honest and ethical manner, without any sort of plagiarism and misconduct, which is taken very seriously by the university and will result in consequences. NTNU can use the results freely in research and teaching by proper referencing, unless otherwise agreed.

The thesis shall be submitted with an electronic copy to the main supervisor and department according to NTNU administrative procedures. The final revised version of this thesis definition shall be included after the title page. Computer code, pictures, videos, dataseries, etc., shall be included electronically with the report.

Start date: 15 January, 2021   **Due date:**   As specified by the administration.

Supervisor: Roger Skjetne
Co-advisor(s):   Zhengru Ren (postdoc) and Namireddy Praveen Reddy (PhD)

Trondheim, February 15, 2021

_____
Roger Skjetne
Supervisor

Preface

This thesis is written to fulfill the graduation requirements for the International Master's program in Marine Technology at the Norwegian University of Science and Technology (NTNU) during the spring semester of 2021.

Trondheim June 9th 2021

Yuxuan Cai

Acknowledgment

I would like to thank my supervisor, Roger Skjetne, for offering me this thesis topic and the thesis guidelines. Also, thanks also to my co-supervisor, post-doctor candidate Zhengru Ren, for his constructional advice on my thesis writing. Special thanks to my co-supervisor, Ph.D. candidate Namireddy Praveen Reddy. This thesis would not have been possible without his support and patience.

In addition, I am much grateful to Daniel Albert, who is always standing behind me, giving me encouragement and patience throughout the thesis.

Trondheim June 9th 2021

Yuxuan Cai

Abstract

Battery energy storage system (BESS) is widely applied in hybrid-electric and all-electric power and propulsion solutions to reduce fuel consumption and emissions in ships. To achieve optimal performance, it is necessary to estimate and monitor the conditions of the BESS, such as state-of-charge (SOC) and state-of-health (SOH). Moreover, to ensure a safe operation, the failure of batteries should be predicted, and the faults in a BESS should be detected and handled.

This thesis focuses on a model-based and data-driven-based method for both condition monitoring and fault detection. Due to the lack of available datasets in the marine industry, two public Li-ion battery datasets from the electric vehicle industry are adopted. It should be noted that the obtained results would be equally applicable in the marine industry. The short-term drive cycle performance dataset is used for: a) SOC estimation with extended Kalman filter (EKF) and recurrent neural networks (RNN) with long short-term memory (LSTM), b) power limit estimation with hybrid power pulse characterization (HPPC), and c) voltage sensor fault detection. The long-term degradation dataset is used for a) SOH estimation and b) remaining useful life (RUL) prediction.

For SOC estimation, the EKF achieved an average mean absolute error (MAE) of 0.64% on nine drive cycles, while the LSTM-RNN, which used current and voltage as input features, had an MAE of 0.84% on the test set. For power limit estimation, the HPPC method showcased how power limit can be determined based on SOC and terminal voltage. For SOH estimation and RUL prediction, the LSTM-RNN, which used cycle number and features of the incremental capacity (IC) analysis as input features, achieved an MAE of 0.62% in SOH estimation and 64.7 cycles in RUL estimation. For fault detection, the generalized likelihood ratio (GLR) algorithm provides a systematic approach for residual analysis. Test results showed that the GLR decision function is capable of detecting voltage sensor faults with a short time delay of 0.3s.

Key words: Battery energy storage system (BESS), condition monitoring, fault detection, recurrent neural network (RNN), long short-term memory (LSTM), state-of-charge (SOC) estimation, state-of-health (SOH) estimation

Contents

List of Figures

List of Tables

Acronyms

BESS battery energy storage system. 1

BMS battery management system. 2

CAN control area network. 10

CUSUM cumulative sum. 62

ECM equivalent circuit model. 1, 2

EIS electrochemical impedance spectroscopy. 49

EKF extended Kalman filter. 2, 25

EMS energy management system. 10

EOL end of life. 14, 47

ESR equivalent series resistance. 48

EV electric vehicle. 10

GLR generalized likelihood ratio. 3, 62

HPPC hybrid pulse power characterization. 2, 49

IC/DV incremental capacity/differential voltage. 51

KF Kalman filter. 1, 22

Li-ion Lithium-ion. 5

LSTM long short-term memory. 2, 25

NiMH nickel-metal hydride. 5

OCV open-circuit voltage. 17

Chapter 1

Introduction

1.1 Motivation

During the last decade, enabling technologies in energy storage, especially battery-based systems, have resulted in new hybrid-electric and pure battery-electric power and propulsion solutions to reduce fuel consumption and emissions in ships. Mixing diesel-generators and battery energy storage system (BESS) in a hybrid power system enable various control strategies, such as spinning reverse, peak shaving, load leveling, and energy harvesting.

To use the battery in a safe and optimal manner, exact information of charges, health, discharge and charge rates, power limit, and failure symptoms, are necessary to be estimated , predicted, and monitored. Furthermore, faults must rapidly be detected.

The main objective of this project is to study state-of-the-art BESS solutions related to battery condition monitoring, involving relevant states and state estimation methods for the critical BESS parameters, including failure prediction and detection. Of particular interest is to study machine learning methods and compare these to more traditional Kalman filter (KF) methods on equivalent circuit model (ECM).

1.2 Scope and limitations

The thesis should cover the following scope of work:

- Perform a background and literature review to provide information adn relevant references on:
  - Marine battery storage solutions including parts, control functions, and auxiliaries.
  - Battery parameters and related models for condition monitoring and control, in particular methods/algorithms for state-of-charge (SOC) and state-of-health (SOH) estimation, failure prediction, and fault detection.
  - Relevant physics-based (model-based) and data-driven methods (machine learning methods) for the estimation, prediction, and detection problems.

○ Relevant datasets, if this can be found.

- Implement and test estimation methods, comparing data-driven methods with estimation based on equivalent circuit model (ECM), particularly KF-based methods, considering:

   ○ SOC estimation,
   ○ power limit estimation, and
   ○ SOH estimation

Analyze and discuss the resulting performance of each problem and method.
- Present and discuss the common faults that may occur in a BESS. Present the crucial parameters/indicators and relevant models to identify these faults.
- Propose, implement, and test relevant method(s) related to fault detection for BESS. Analyze and discuss the resulting performance.

The limitations of the works include

- Currently there are no available public datasets from the marine industry. Two public Li-ion datasets from the EV industry are adopted in this thesis.
- Fault data are not included in the original datasets. Thus, for fault detection purpose, the data are manipulated to simulate faults.
- The discussion over marine battery products on the current market is limited due to the lack of information.

1.3 Thesis organization

The structure of the thesis is shown as follows:

- Chapter 2 starts from the principle of operation of a single battery cell and the comparison of various battery chemistries. Then, the BESS solution, topology, and functions are introduced. As an important part of a BESS, the functional roles of a battery management system (BMS) are also presented. Last but not least, a case study on all-electric ferries in service is performed.
- Chapter 3 first presents the terms that are important for battery modeling. Subsequently, the physics-based battery model and the ECM are both introduced, where the ECM will be the main focus of this thesis.
- Chapter 4 summarizes the common methods for SOC estimation and applies the extended Kalman filter (EKF) and the recurrent neural network (RNN) with long short-term memory (LSTM) cells for SOC estimation.
- Chapter 5 first presents a standard method to estimate power limit - the hybrid pulse power characterization (HPPC). Subsequently, the enhanced HPPC based on the proposed ECM model is introduced and implemented.
- Chapter 6 summarizes the available methods to estimate battery SOH and remaining useful life (RUL). The LSTM-RNN is again utilized to evaluate battery health in this chapter.

- Chapter 7 lists various faults that can occur in a Li-ion BESS and also summaries methods for fault detection. Based on the EKF, voltage sensor faults can be detected via residual analysis. The threshold for the residual analysis is determined by the generalized likelihood ratio (GLR) algorithm.
- Chapter 8 summarizes the results and findings in this thesis and gives suggestions for further research work.

Chapter 2

Marine Battery Energy Storage System

2.1 Battery technology

Before studying a large-scale battery system, it is essential to understand how a battery cell works and to know different types of battery. Also, this section will introduce the technical specifications for a battery and application requirements for various ship types.

2.1.1 Principle of operation
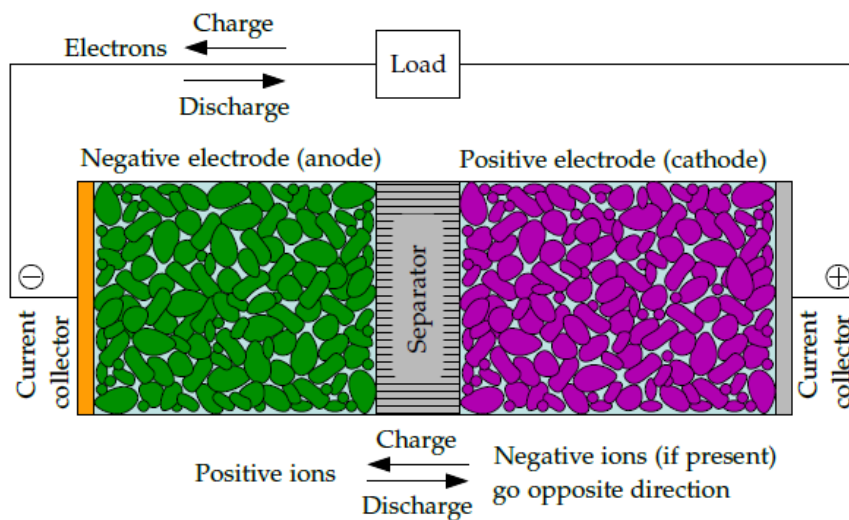
Figure 1: Schematic diagram of a battery cell (Plett 2015*b*)

A battery converts chemical energy into electrical energy using redox reactions be-

tween the positive electrode (cathode) and the negative electrode (anode).

During discharge, the negative electrode releases electrons to the positive electrode via the external circuit, while during charge, the negative electrode receives electrons from the positive electrode in the same way. These chemical processes are called reduction-oxidation (redox) reactions.

Within the battery cell, however, the process is different. During discharge, the cations move through the electrolyte - an ionic conductor that provides the medium for internal ion transfer - towards the positive electrode, while the anions move towards the negative electrode. During charge, the opposite process occurs. Between the negative electrode and the positive electrode, there is an electronic insulator called a separator. It can prevent internal short-circuit and subsequent faults, which will be discussed in Chapter 7.

2.1.2 Battery chemistry

In terms of rechargeability, batteries can be classified into primary batteries and secondary batteries, while the latter is of particular interest in marine applications. Secondary batteries are also known as rechargeable batteries, where the internal chemical reactions can be reversed by applying electric current during the charging process.

Secondary batteries can be further divided into several types depending on the anode/cathode materials. Common types include lead-acid, nickel-metal hydride (NiMH), and Lithium-ion (Li-ion). A comparison of battery types is listed in Table 1. This section is based on the work in *Types of Lithium-ion* (n.d.) and Helgesen et al. (2019).

Table 1: Specifications for different types of batteries (Helgesen et al. 2019)

Specification		Specific energy (Wh/kg)	Nominal voltage (V)	Cycle life	Applicable for maritime
Lead-acid		30-50	2.0	200-300	
NiMH		60-120	1.2	300-500	
Li-ion	LCO	150-200	3.6	500-1000	
	LFP	90-120	3.3	1000-2000	Yes
	NMC	150-220	3.6	1000-2000	Yes
	LMO	100-135	3.3	300-700	
	NCA	200-260	3.6	500-1000	Yes

Lead-acid battery

As the first generation of secondary batteries, lead-acid batteries are still the most commonly used type in boats and vehicles due to their low cost and high power output

capability. Also, it is considered to be very safe, as the electrolyte and active materials are not flammable. However, the specific energy of lead-acid batteries is very low, and thus they are usually heavy.

Nickel metal hydride battery (NiMH)

NiMH has a higher power density than a lead-acid battery, and the cost of the batteries is low.

Both internal resistance and self-discharge rate are high, and thus the cycle life is relatively low compared to a lithium-ion battery. Besides, hydrogen gas is released during charge, which leads to the potential to create an explosive atmosphere.

Lithium cobalt oxide, $LiCoO_2$ (LCO)

As the first application of lithium-ion battery, it has relatively high energy density. LCO is widely applied in consumer electronics within a three-year life span. However, its short life cycle and low power rate limit its applications in maritime.

Lithium iron phosphate oxide, $LiFePO_4$ (LFP)

The cathode's high stability reduces the risk of thermal runaway and makes it resilient to temperature fluctuations.

Disadvantages for LFP include relatively low specific energy, lower voltage, and lower power capabilities.

Lithium nickel manganese cobalt oxide, $LiNiMnCoO_2$ (NMC)

With the combination of attributes of the constituents of nickel (high specific energy), cobalt (high specific energy), and manganese (provides structure stability), NMC becomes the most used chemistry in marine applications at present. The composition of the elements can be adjusted and customized based on needs.

NMC is preferred for electric vehicles and within the maritime industry as its life cycle is long while the energy density is satisfying (*Batteries on board ocean-going vessels* n.d.).

Lithium nickel cobalt aluminum oxide, $LiNiCoAlO_2$, (NCA)

As a further development of LCO, NCA with additional aluminum has the highest specific energy in the Li-ion battery clan. The outstanding specific energy makes it suitable for marine applications.

2.1.3 Technical specifications

This section presents the specifications on battery technical specification sheets. These specifications are used extensively in the following chapters, and thus it is crucial to define them. The following definitions are adapted from MIT (2008).

- **Nominal voltage (V).** The reference voltage of the battery provided by the man-

ufacturer.

- **Cut-off voltage.** The minimum allowed voltage. When a battery is at its cut-off voltage, it is usually considered as empty.
- **Nominal capacity (Ah).** The total Amp-hours available when the battery is discharged at a specific C-rate from 100% SOC to the cut-off voltage.
- **Nominal energy (Wh).** Similar to the nominal capacity, the total Watt-hours available when the battery is discharged at a certain C-rate from 100% SOC to the cut-off voltage.
- **Cycle life.** The number of discharge-charge cycles the battery can experience before it fails to meet its EOL. Cycle life is a number for a particular DOD. Usually when the DOD is high, the cell degrades quickly and it leads to a lower cycle life.

2.1.4 Battery application feasibility and requirements for various ship types

For maritime applications, various ship types have different operational profiles, and thus the battery application may vary. Generally speaking, batteries have not yet been utilized on a large scale in maritime applications. The main restriction is that the specific energy and power cannot meet the demand of such applications. As of now, the only battery-only application is on ferries, which has a relatively short route and a long time on the port to charge. In other vessels, batteries are usually utilized for spinning reserve, peak shaving, or silent operation. Table 2 by Helgesen et al. (2019) gives an overview of main battery function and battery requirements for various ship types.

Table 2: Application feasibility and battery requirements for various ship types

Ship type	Main battery function	Battery requirements		
		C-rate	Cycles	Energy
Ferry	All electric	Very high	Very high	Nominal
Offshore supply vessel	DP - Spinning reserve	Very high	Very low	Medium
Cruise	Hybrid operating in all electric	Low	High	Very high
Offshore drilling vessel	Spinning reserve and peak shaving	Very high	Variable	Low
Fishing vessel	Hybrid load levelling and spinning reserve	Medium	Medium	Medium
Yachts	Silent operation, spinning reserve	Low	Low	High

2.2   BESS topology and functions

For the longest time, the BESS has been utilized in ships as an uninterruptible power supply (UPS) for emergencies. Thanks to the development of technologies, the BESS has been widely used as an auxiliary or even main power source because of its benefits, which are listed in section 2.2.3. Also, section 2.2.2 shows the system topology for BESS in both hybrid propulsion ships and all-electric propulsion ships.

2.2.1   Battery pack topology

With the discussion in the previous section, we know the voltage for different battery chemistries is fixed in specific ranges, usually 3-4V. The maximum current for a cell is usually 20-30A. Thus the power provided by a single cell is roughly 60-120W. However, for a BESS on a ship, the required power can reach thousands of kilowatts. To achieve high power, battery cells in a battery pack are organized to generate high current and high voltage.

There are two types of electric circuits: series circuits and parallel circuits. When cells are connected in series, the pack voltage is the sum of the individual cell voltages. Assume all cell voltages are equal, we have $v_{pack} = N_s \times v_{cell}$, where N_s is the number of cells in series. Similarly, when cells are connected in parallel, the pack current is the sum of the individual cell currents. With the assumption that all cell currents are equal, we have $i_{pack} = N_p \times i_{cell}$, where N_p is the number of cells in parallel.

For EV applications, a battery module, which consists of groups of cells, are usually designed to have maximum voltage less than 50V for safety concern. A battery pack voltage is usually kept to less than 600V, because power electronics that operate at higher voltages are expensive (Plett 2015*b*).

For maritime applications, a containerized BESS solution is proposed by Corvus Energy(*Corvus Energy introduces standardized ISO footprint containerized battery room solutions* 2021), ABB(*ABB Containerized maritime energy storage* n.d.), and Eaton(*Eaton Containerized energy storage system* n.d.). Such a containerized BESS has a capacity up to 2MWh. It has the advantages such as flexibility, high efficiency, and easy installation. It is a suitable solution for offshore supply vessels and other applications with huge power consumption.

2.2.2   Ship power and propulsion system

Hybrid propulsion ship

Figure 2(a) depicts a propulsion ship with batteries integrated into the power system. The batteries can provide power to the large propulsion motors. The hybrid propulsion ship may run on the generators only, the batteries only, or on both the generators and the batteries. The batteries can connect either directly to the thrusters with converters or to the electric bus. A distributed configuration can reduce the number of converters, and thus the loss caused by converters can be reduced as well.

(a) Propulsion system configuration for a hybrid ship

(b) Propulsion system configuration for an all-electric ship
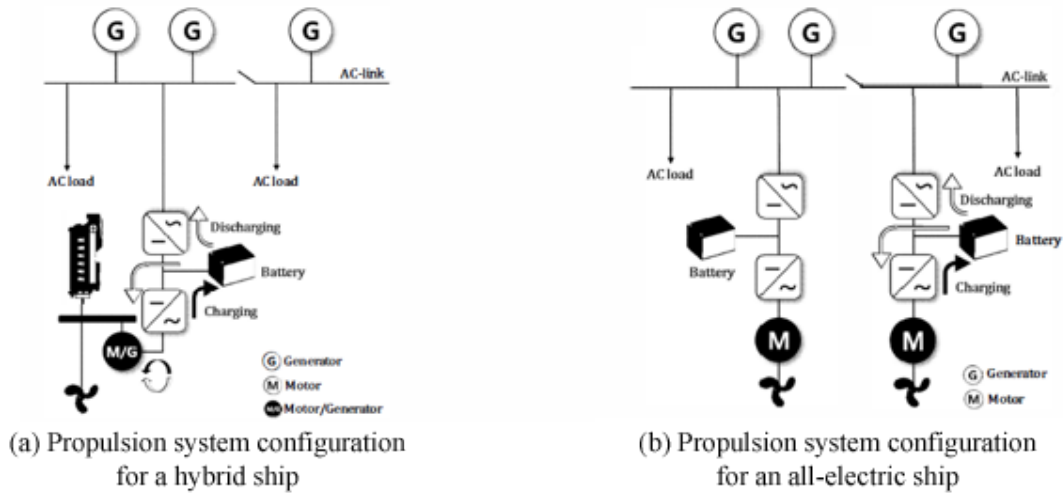
Figure 2: BESS topology on ships (Kyunghwa Kim et al. 2016)

A hybrid energy solution can reduce the operational noise and vibration level on the ship. Also, as a supplemental source for propulsion, the batteries can smooth the load variations on the generator sets.

All-electric propulsion ship

Fig. 2(b) depicts a propulsion ship with pure battery-driven power system. The BESS is charged through an AC/DC converter, which can be located either on the vessel or on shore. According to class rules, two independent BESSs should be installed to provide propulsion power if one of the systems fails (*Rules for classification - ships* 2019a).

2.2.3 BESS functions on ships

According to Helgesen et al. (2019), BESSs on ships can have multiple functional roles summarized as follows:

- **Spinning reverse.** A BESS can be a backup for running generators. In this case, fewer generators are required online simultaneously.
- **Peak shaving.** A BESS moderates electricity demands and reduces the peaks as a buffer. The energy stored in a BESS can compensate for the peak hours, which usually last for a short duration.
- **Load leveling.** A BESS stores power when there is a light loading on the power system and delivers it during high demand (Mutarraf et al. 2018).
- **Energy harvesting.** In some applications, the load can generate power which can be utilized to charge the batteries. A BESS can capture energy from these applications, such as crane operations, drilling equipment, etc.
- **Backup power.** Traditionally, a BESS works as an UPS for emergencies. A UPS

is "used to protect hardware such as computers, telecommunication equipment or other electrical equipment where an unexpected power disruption could cause data loss, injuries, or even fatalities." (*Uninterruptible power supply* n.d.)

2.3 Battery management system (BMS)

Lu et al. (2013) gives a straightforward definition of a BMS, "any system that manages the battery." According to the definitions in *Rules for classification - ships* (2019*b*), a BMS is "a collective terminology comprising control, monitoring and protective functions of the battery system." Despite the fact that there is no universally agreed-upon definition of it, based on the works of Plett (2015*b*), Lu et al. (2013), and *Rules for classification - ships* (2019*b*), a BMS is usually expected to have the following functions:

- **Sensing.** A BMS should consecutively measure voltage, temperature, and current both on a cellular level and a pack level. The three parameters are essential for state estimation and fault detection.
- **Codition monitoring.** state-of-charge (SOC), state-of-health (SOH), and power limit should be estimated and be available for the energy management system (EMS). Also, the remaining useful life (RUL) is an important indicator for battery failure and should be predicted as well. According to Helgesen et al. (2019), methods for estimating SOC and SOH should be based on industrial practice for the relevant battery technology. Such methods may use a combination of measurements and prediction algorithms. Factors such as battery characteristics, operating temperature, charge/discharge rate, self-discharge, and cell aging should be considered. Chapter 4, 5 and 6 will provide deeper insights into this topic.
- **Fault detection.** Common faults for a cell can be classified into internal faults and external faults. Based on the measurements and estimates, the BMS should be able to detect fault occurrence to prevent safety hazards. Chapter 7 will present common faults for a cell, methods for detection, and algorithm test results.
- **Protection and control.** When faults are detected, the BMS should use electronics and logic to protect the batteries from faults such as overcharge, overdischarge, over current, short circuits, extreme temperature, etc. Control includes thermal control, charge control, and cell balancing.
- **Log book and communication.** Key data, such as SOC, SOH, number of cycles completed, and fault code should be stored by the BMS for warranty and diagnostic purposes. The BMS should also be able to communicate with other components in the system via a specific protocol. For large BESS on electric vehicle (EV) or ships, a control area network (CAN) is the preferred protocol as it provides robust communications in harsh operating environments with high levels of electrical noise. While for a small application, such as an remotely operated vehicle (ROV), RS232 is sufficient.

2.4 Case study: all-electric ferries
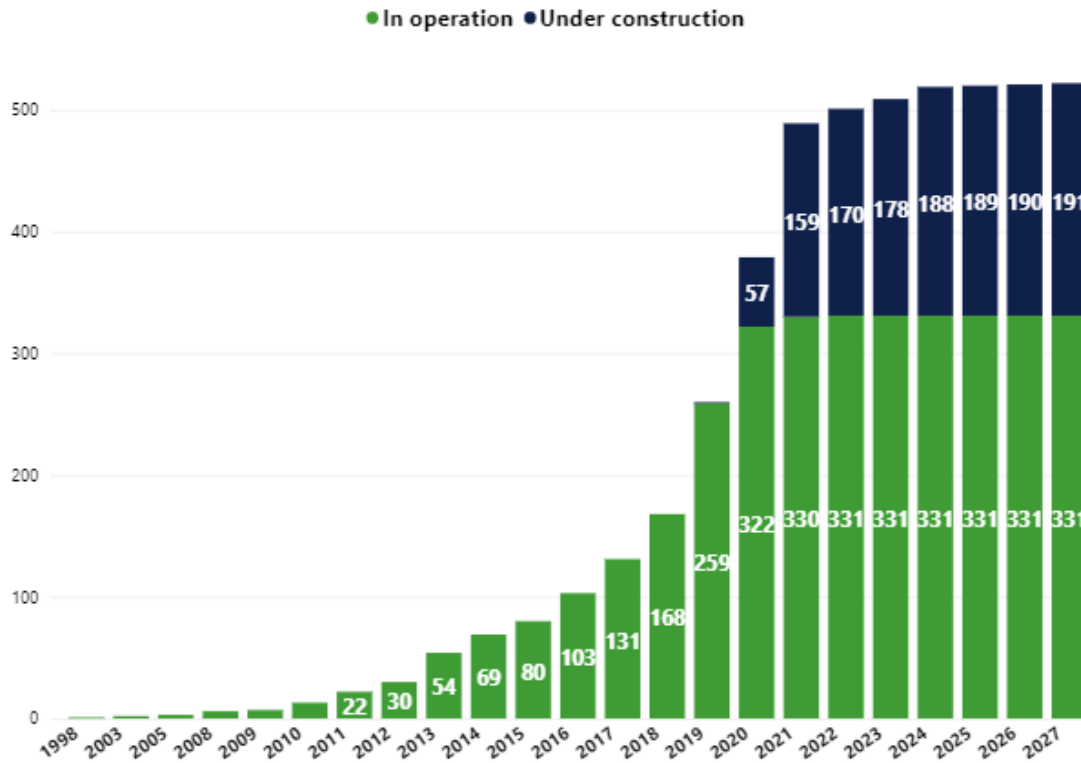
Figure 3: Total number of ships with batteries as of June, 2021. Statistics source: DNV's AFI platform (http://afi.dnvgl.com)

From Fig. 3 and 4, we can see passenger/car ferries are the largest segments where maritime batteries are applied. Ferries have predictable, short, and fixed routes every day, and the staying at the port is relatively long. These characteristics make ferries suitable for all-electric operations. Table 3 summarizes major all-electric ferries in service.

MF Ampere

As the world's first battery-electric ferry, *MF Ampere* operates between Lavik and Oppedal (5.7km, 20 minutes, 34 times per day) in Norway. The 10t lithium-ion batteries have an overall capacity of 1000kWh, which can be charged in 10 minutes between crossings from high-capacity batteries at each port. It saves a million liters of diesel each year, and its operating costs are about 80% lower. Its CO_2 emission is only 5% of those of a conventional diesel ferry (*MF Ampere* n.d.). Since then, an electric ferry revolution swiped the world.

200

150

100

50

0

71													
154	37	11											
	66	54		7	7								10
			12	11	9		18	13	6				

Car/Passenger ferries · Other activities · Offshore supply ships · Tugs · Fishing vessels · Other offshore vessels · Crude oil tankers · Cruise ships · Ro-ro cargo ships · Bulk carriers · RoPax · Container ships · General cargo ships · Oil/Chemical tankers · Car/Passenger ferry
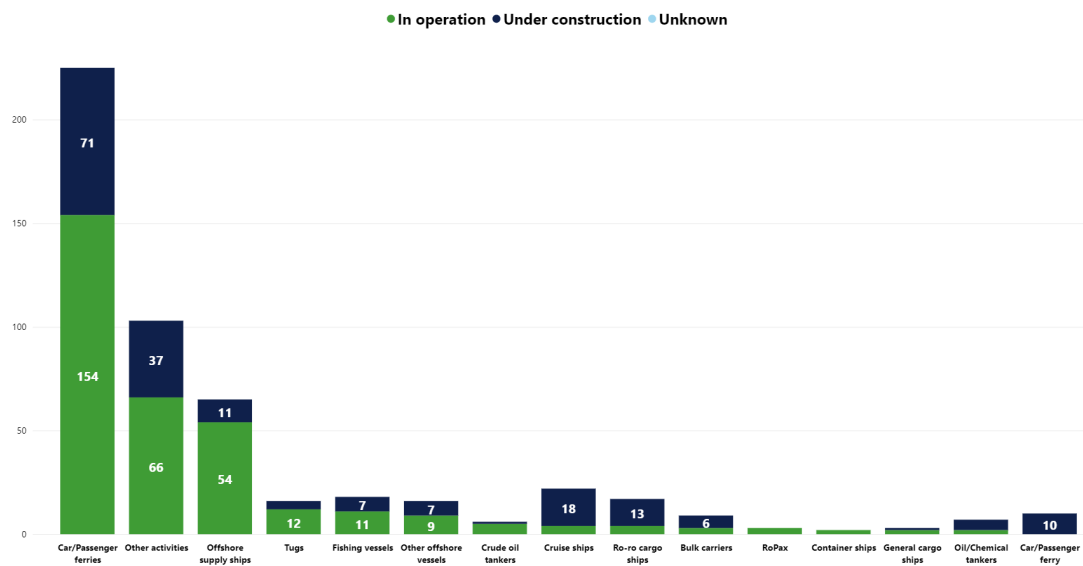
Figure 4: Total number of ships with batteries by ship types as of June, 2021. Statistics source: DNV's AFI platform (http://afi.dnvgl.com)

Ellen

Led by E-ferry project funded by European Commission Horizon 2020, *Ellen* was designed and built to meet the aim of a 100% electrically driven passenger and car ferry. Ellen was built to operate the 22 nautical miles between the islands of Ærø and Als in Southern Denmark, and it is charged only while in Søby. Not only the noise and vibrations are reduced by all-electric operation, but also it is estimated that the ferry will reduce about 2000 tonnes of CO_2, 41500 tonnes of NO_x, 1,35 tonnes of SO_x, and 2,5 tonnes of particles per year (Helgesen et al. 2019).

Tycho Brache and Aurora

Led by the project *Zero Emission Ferries*, the two ferries *Tycho Brache and Aurora* are converted from marine gas oil to plug-in all-electric powered by batteries. They both operate between Helsingør in Denmark and Helsingborg in Sweden. The ferries are charged at each port, which takes about 5-9 minutes with about 1200 kWh (Helgesen et al. 2019).

To date, the typical battery capacities for pure electric car in the US are 67kWh, and for an electric bus in China are 210kWh. On the contrary, electric ships have the largest individual batteries of any electric vehicle sector (Gear 2020). Batteries on electric ships always appear in packs, sometimes even in container size, and the capacities are up to thousands of kWh.

Table 3: Technical details of all-electric ferries (Helgesen et al. 2019)

Name	Capacity	Battery storage capacity	Battery chemistry
MF Ampere	120 cars 350 passengers	1000kWh	NMC
Ellen	31 cars 198 passengers	4.3MWh	NMC
Tycho Brache	240 cars 1250 passengers	4.1MWh	-
Bastø Electric	200 cars 24 trucks 600 passengers	4.3MWh	-

Bastø Electric

Launched in March 2021, the Bastø Electric is the world's largest all-electric ferry. The ferry goes into service in Norway on a 10km-long route between Moss and Horten, across the Oslo Fjord. It is 139.2m long and 21m wide, with a capability of 600 passengers and 200 cars/24 trucks. The batteries on Bastø Electric have a capacity of 4.3 MWh, and the fast-charging system has a capacity of 9 MW. It is estimated that emissions on this ferry route will be reduced by 75% during 2022 (*World's largest electric ferry launches in Norway* 2021).

Oberhaus (2020) summarizes the two major challenges with building electric ships. One is that conventional lithium-ion batteries come with safety risks because of the liquid electrolytes. If the components in a battery degrade or age, this could cause the cell to rapidly heat up and fail, which is usually called thermal runaway. Thermal runaway can lead to undesired consequences, for example, a cascade of failures in nearby batteries. If these batteries release the internal chemicals as they fail, it would even lead to a large explosion.

Another major challenge for electric ships is that conventional lithium-ion battery chemistry does not contain enough power to move cargo worldwide. Nowadays, NMC batteries can only be applied to electric ferries and small container ships. More advanced battery technology is essential to meet the energy demands of massive international cargo ships.

Chapter 3

Battery Modeling

We now know one important function of a BMS is to estimate a number of fundamental quantities, such as SOC, SOH, and power limit. This chapter aims at proposing and comparing two battery models - the physics-based model and the equivalent circuit model - which are widely used for failure mode identification and state estimation. The terms are first and foremost proposed, and they are used repeatedly throughout this thesis.

3.1 Terminology

3.1.1 State-of-charge (SOC)

SOC is an important battery state that indicates the remaining capacity of a cell. It is by convention a percentage between 0% (empty) and 100% (full). The formal definition will be provided in Chapter 4. For a BMS, an accurate estimate of battery cell's SOC is an important input to balancing, energy, and power calculations. Also, an accurate SOC estimate provides several benefits, as Plett (2015*b*) summaries as follows:

- **Longevity.** Over-charging or over-discharging a battery cell may cause permanent damage and result in reduced service time. An accurate SOC estimate can be applied to avoid harming cells by not permitting current to be passed.
- **Performance.** With a good SOC estimate, especially with known error bounds, one can aggressively use the total cell capacity.
- **Reliability.** A good SOC estimator is consistent and dependable for any driving profile, enhancing overall power system reliability.

3.1.2 State-of-health (SOH)

State-of-health is a slow varying state for a battery cell, indicating the aging degree of a cell. Although it is by convention a percentage from 0% to 100%, when SOH drops below 80%, it is usually considered as the end of life (EOL) of a battery and the battery should be replaced. The formal definition of SOH will be proposed in Chapter 6.

The most significant purpose of monitoring SOH is one would know when to replace

the battery, as aging of a battery would diminish its performance and increase its temperature during operation. The latter is a potential hazard to the system's safety.

3.1.3 C-rate

For batteries, charge/discharge current is often expressed as a C-rate, aiming to normalize against battery capacity, as battery capacity varies differently between batteries. A C-rate measures the rate at which a battery is discharged relative to its maximum capacity (MIT 2008).

For example, a 1C rate means the current will charge/discharge the entire battery in 1 hour. Also, using the relation between capacity and C-rate, we can calculate the discharge current as well. For a 1C rate battery with a capacity of 2.9Ah, this is equivalent to a discharge current of 2.9A.

3.1.4 Depth-of-discharge (DOD)

DOD is the percentage of battery capacity that has been discharged. It is expressed as a percentage of maximum capacity. A discharge to at least 80% DOD is referred to as a deep discharge (MIT 2008). The relationship between DOD and SOC is

$$\text{DOD} = 100\% - \text{SOC} \tag{3.1}$$

3.2 Physics-based model (PBM)

The PBM is based on the electrochemical processes inside the cell. This type of model describes all internal cell processes using coupled partial differential equation (PDE). The equations presented in this section are for a continuum-scale model, which describes behaviour in the neighborhood of a spatial location using a volume average of an underlying microscale model. We assume a simplified one-dimensional cell geometry where all electrode solid particles are spherical, as is depicted in Fig. 5. This section is adapted from Plett (2015*b*).
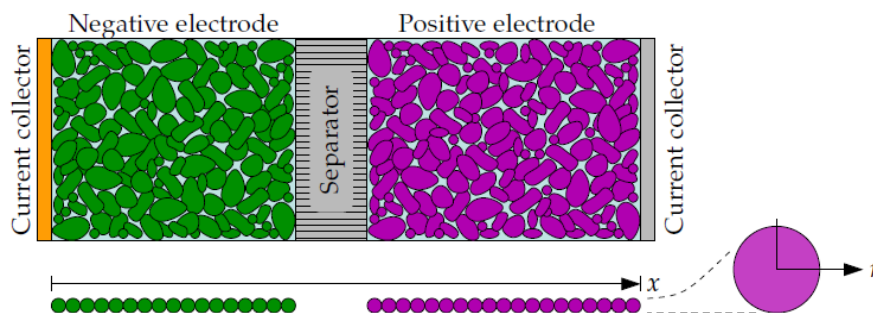
Figure 5: Illustration of PBM (Plett 2015*b*)

15

Before introducing the PDEs, it is essential to explain the variables involved:

- $c_s(x, r, t)$: the concentration of lithium in the solid active materials that comprise each electrode at spatial location x across the cell and at radial location r within a particle.
- $c_{s,e}(x, t)$: the concentration of lithium at the solid-electrolyte boundary at the surface of the solid.
- $\phi_s(x, t)$: the electric potential in the solid.
- $\phi_e(x, t)$: the electric potential in the electrolyte.
- $j(x, t)$: the flux density between solid and electrolyte.

The five variables can be found by solving four coupled continuum-scale PDEs and one algebraic equation.

- To determine the concentration of lithium in the spherically symmetric solid electrode particles,

$$\frac{\partial}{\partial t} c_s = \frac{D_s}{r^2} \frac{\partial}{\partial r} \left(r^2 \frac{\partial c_s}{\partial r} \right) \tag{3.2}$$

  where D_s is the solid diffusivity.
- Charge balance in the solid active material particles,

$$\nabla \cdot (\sigma_{\text{eff}} \nabla \phi_s) = a_s F j \tag{3.3}$$

  where σ_{eff} is the effective electronic conductivity of the electrode materials in the porous electrode and a_s is the specific interfacial surface area of the electrode active materials.
- Mass balance of lithium in the electrolyte,

$$\frac{\partial (\varepsilon_e c_e)}{\partial t} = \nabla \cdot (D_{e,\text{eff}} \nabla c_e) + a_s \left(1 - t_+^0 \right) j \tag{3.4}$$

  where ε_e is the porosity of the electrode, $D_{e,\text{eff}}$ is the effective diffusivity of the electrolyte and t_+^0 is the transference number of the positively charged lithium ion with respect to the solvent in the electrolyte.
- Charge balance in the electrolyte,

$$\nabla \cdot (\kappa_{\text{eff}} \nabla \phi_e + \kappa_{D,\text{eff}} \nabla \ln c_e) + a_s F j = 0 \tag{3.5}$$

  where κ_{eff} is the ionic conductivity of the electrolyte and $\kappa_{D,\text{eff}}$ is the ionic conductivity multiplied by a conversion factor.
- The Butler-Volmer equation to determine the rate of reaction at the surface of the

particles,

$$j = k_0 c_e^{1-\alpha} \left(c_{s,\text{max}} - c_{s,e} \right)^{1-\alpha} c_{s,e}^{\alpha} \left\{ \exp\left(\frac{(1-\alpha)F}{RT} \eta \right) - \exp\left(-\frac{\alpha F}{RT} \eta \right) \right\} \quad (3.6)$$

where η, k_0 are the reaction-rate constant and α is the asymmetric charge-transfer coefficient.

Compared to the ECM, the PBM can predict over a wide range of operating conditions and predict the cell's internal electrochemical state. Therefore, it is useful for aging prediction and failure mode identification. However, such a model requires a considerable amount of computational effort as it is expressed in PDE, which also brings robustness and convergence issues. In real-time applications such as a BMS, PBM is not applicable due to the limitations of computational capability. Throughout the thesis, the main focus is on the ECM. Thus the PBMs are only briefly introduced. To obtain more insight into PBMs, one may refer to Plett (2015*b*).

3.3   Equivalent circuit model (ECM)
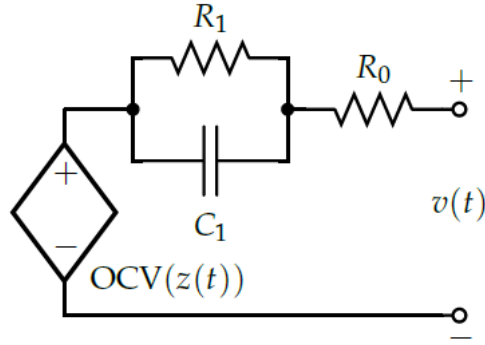
Figure 6: ECM model (Plett 2015*a*)

A lithium-ion battery cell's input/output behaviors are usually simplified with an ECM, comprising a voltage source, resistors, and capacitors. The cell itself does not contain these electronic components, but its output (voltage) response to an input (current) resembles one produced by the circuit model. Compared to the physics-based model, which describes all internal cell processes using the partial differential equation, the ECM is used extensively as the basis for real-time control algorithms in commercial battery packs because of its simplicity and computational efficiency.

Fig. 6 depicts the ECM model used throughout this thesis. The model consists of a controlled voltage source $\text{OCV}(z(t))$, an equivalent series resistance R_0 and one RC pair R_1 and C_1. Generally, the open-circuit voltage (OCV) of a cell is a function of SOC and temperature, and this will be discussed further in later sections. The diffusion process

within a lithium-ion cell is referred as a diffusion voltage, and its behaviors can be approximated using one or more RC pairs. For simplicity, only one RC pair is considered in the model.

Constants R_0, R_1, C_1, and so forth are called *model parameters*. As they are imaginary components, there exists no direct method to measure them. However, based on the cell data, they can be adjusted using an optimization procedure. This process is called *system identification*. For further discussion, see Section 3.4.

The proposed ECM model comprises two states:

State-of-charge. SOC at a time step k is denoted as z_k. It is well defined in Chapter 4.

Diffusion resistor current. Current through the diffusion resistor R_1 at time step k is denoted as $i_{R_1,k}$ and is defined as

$$i_{R_1,k+1} = \exp\left(\frac{-\Delta t}{R_1 C_1}\right) i_{R_1,k} + \left(1 - \exp\left(\frac{-\Delta t}{R_1 C_1}\right)\right) i_k \tag{3.7}$$

Note that the input to the system is current i_k. If we define $A_{RC} = \exp\left(\frac{-\Delta t}{R_1 C_1}\right)$, the overall state-space equation can be expressed as

$$\begin{bmatrix} z_{k+1} \\ i_{R,k+1} \end{bmatrix} = \begin{bmatrix} 1 & 0 \\ 0 & A_{RC} \end{bmatrix} \begin{bmatrix} z_k \\ i_{R,k} \end{bmatrix} + \begin{bmatrix} -\frac{\eta_k \Delta t}{Q} \\ 1 - A_{RC} \end{bmatrix} i_k. \tag{3.8}$$

With the Kirchhoff voltage laws, the output v_k at time step k is expressed as

$$v_k = \text{OCV}(z_k) - R_1 i_{R_1,k} - R_0 i_k \tag{3.9}$$

The battery cell models are essential for state estimation, parameter estimation, as well as fault detection. Chapter 4, 6 and 7 will provide a comprehensive insight into each topic.

3.4 System identification

In general, it requires two tests to identify the parameters of a battery model: an OCV test and a dynamic test. These two tests are performed in laboratory with battery-cell cyclers, and the general process is presented in Fig. 7. Plett (2015a) introduces the system identification process and this section is based on his works. This section describes the general ideas of these tests, and the dataset that is used for SOC estimation (Chapter 4), power limit estimation (Chapter 5), and fault detection (Chapter 7) in this thesis.
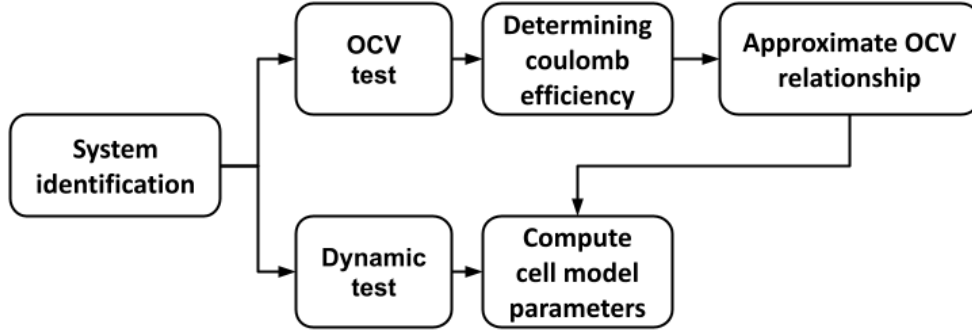
Figure 7: System identification process

3.4.1 OCV test

The test procedure is straightforward. In order to minimize the excitation of the dynamic components of the cell model, the cell is charged/discharged at a very low rate (C/20), while measuring cell voltage and accumulated ampere-hours discharged. In this way, the voltage measurement can be approximated as the OCV, i.e., $v_k \approx OCV(z(t))$.

It takes three steps to process the experimental data. First, determine the coulombic efficiency. It is noticed that the net number of ampere-hours charged over all steps is higher than the total capacity. That is because the coulombic efficiency when charging is not perfectly 1. Thus, we compute the coulombic efficiency as

$$\eta = \frac{\text{total ampere-hours discharged at all instants}}{\text{total ampere-hours charged at all instants}} \qquad (3.10)$$

Note that the coulombic efficiency is a function of temperature so the result is only valid at a certain temperature.

Next, determine the charge and discharge voltage. As the accumulated ampere-hours measurement is recorded at each time step, we can easily compute the corresponding SOC using the definition. Note that the measurement denotation might differ during charging and discharging and it is important to take that into account when processing the data. Finally, because the OCV profile during charging and discharging are different, we have to approximate the relationship based on the two curves.

As a cell's OCV is a static function of its SOC and temperature, this test is valid at a certain temperature. To obtain OCV relationships at different temperatures, multiple tests should be performed.

3.4.2 Dynamic test

Once we have obtained the OCV relationship, we can move on to find out the parameters of the cell model. During the dynamic test, the cell is charged/discharged at a constant current (C/1) to excite the dynamic components. Voltage, current, temperature, ampere-hours charged, and ampere-hours discharged are recorded every second. With these data, we wish to find parameter values for R_0 and R_1. The residual between output measurement and OCV can be expressed as

$$\tilde{v}_k = v_k - OCV(z_k) = -R_1 i_{R_1,k} - R_0 i_k$$

where $i_{R_1,k}$ can be determined with subspace system identification, and i_k is the input. Then, using least-squares solution, we can find the unknown parameters $R0$ and $R1$.
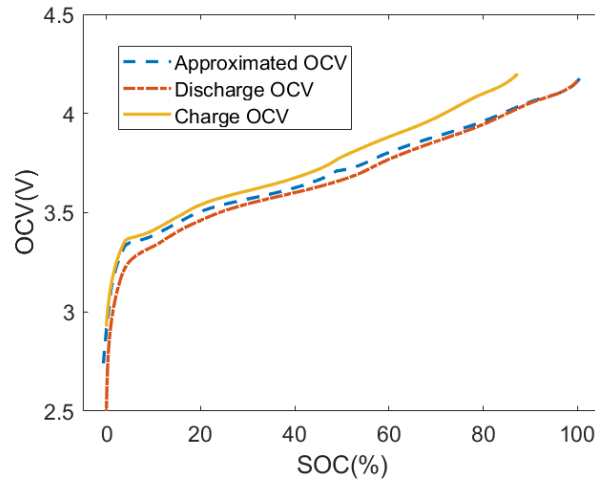
Figure 8: Voltage from OCV tests and the approximate OCV

3.4.3 Dataset used

In Chemali et al. (2017), a 2.9 Ah Panasonic NCA 18650PF cell was tested in a thermal chamber under varying conditions. The cell specifications can be found in Table 4.

The tests included cycles at 1C, at C/20, and a series of nine drive cycle tests. The drive cycles used one, or a mix of US06, HWFET, UDDS, LA92, and a custom neural network drive cycle. This dataset is suitable for system identification as it contains both OCV tests and dynamic tests (BatteryBits 2020). Also, it has a relatively large amount of data, which can be later used for machine learning. Other available datasets either lack both tests for cell modeling or have only one or two drive cycles, far from enough for a machine learning algorithm.

The system identification is based on the ESC toolbox from Plett (2015*a*). The first

Table 4: Panasonic 18650PF cell specifications (Chemali et al. 2017)

Nominal open circuit voltage	3.6 V
Capacity	Min. 2.75 Ah/Typ. 2.9 Ah
Min/max voltage	2.5 V/4.2 V
Minimum charging temperature	10 °C
Cycles to 80% capacity	500 (100% DOD, 25 °C)

step in the implementation process is to identify the OCV relationship. With the OCV test data included in the dataset, we approximate the OCV curve and it is shown in Fig. 8. Using the OCV relationship and the dynamic test data, the parameters of the cell model are identified using least-square regression. The model parameters are as follows: $R0 = 32\text{m}\Omega, R1 = 37.8\text{m}\Omega, C1 = 4.47\text{F}, \eta_k = 0.97, Q = 2.8\text{Ah}$.

Chapter 4

State-of-Charge Estimation

SOC estimation is crucial to the safe and reliable operation of Li-ion battery packs, which become widely used in EVs, smart grid systems, and all-electric ships. SOC is the most critical state for a BMS as it is required as input to balancing strategies and to both energy and power calculations (Plett 2015*b*). However, there is no direct way to measure SOC, making SOC estimation a cumbersome task for a BMS.

In this chapter, Section 4.1 will showcase the definition of SOC and the equivalent circuit model of battery cells. Section 4.2 will present four major methods for SOC estimation: open-circuit method, coulomb counting, Kalman filter (KF), and machine learning, while the latter two will be the main focuses, and they will be discussed successively in Section 4.3 and 4.4.

4.1 Definition

By definition, the SOC of the cell is the ratio of the residual capacity to the total capacity of the cell. In this case, the SOC is defined as

$$z = \frac{Q_{res}}{Q} \times 100\% \tag{4.1}$$

where Q_{res} is the residual capacity and Q is the total capacity. Q_{res} and Q are measured in either mAh or Ah. In applications, the following definitions in both continuous and discrete domain are equivalent and more common

$$z(t) = z(0) - \frac{1}{Q} \int_0^t \eta(t)i(t)dt \tag{4.2}$$

$$z_{k+1} = z_k - \eta_k i_k \frac{\Delta t}{Q} \tag{4.3}$$

where η are the coulombic efficiency at time step k (assumed $\eta = 1$ for discharge and $0 < \eta \leq 1$ for charge), i is the instantaneous cell current (assumed positive for discharge and negative for charge), Δt is the sampling period. As SOC is a percentage, the units of i and t should be able to cancel out the unit of Q.

4.2   SOC estimation methods

In this section, four SOC estimation methods are compared and discussed, including the open-circuit-voltage method, coulomb counting, KF, and machine learning. Table 5 summarizes the methods mentioned and their main characteristics. The following discussion is based on the works of Plett (2015*b*), Ng et al. (2020) and Lu et al. (2013).

Table 5: Summary of SOC estimation methods

Methods	Measurements required	Advantages	Disadvantages
OCV method	Voltage	Easy to implement	Poor accuracy
Coulomb counting	Voltage and current	Easy to implement	Measurement noise, initialization problem
Kalman filter	Voltage and current	High accuracy, roubustness	Model required, computationally intensive
Machine learning	Voltage, current (and temperature)	High accuracy, no need for model	Data availability, huge amount of training time

4.2.1   Open-circuit-voltage (OCV) method

The terminal voltage of a cell is a function of its SOC and current. However, if the cell is at rest, i.e. $i_{R_1,k} = i_k = 0$, we have a simple relationship $v_k \approx \text{OCV}(z_k)$. Fig. 9 shows the OCV-SOC mapping of a lithium-ion cell. With this relationship, we can compute a cell's SOC given the OCV using $z_k = \text{OCV}^{-1}(v_k)$.

However, this method gives poor accuracy in applications due to two reasons. For one thing, this method is based on the assumption that the cell is at rest, while in applications, the cell is hardly at rest when it is working. This method misses two important terms in the output equation 5.2.1, and thus it is not practical to apply it in real-time estimations. For another, as shown in Fig. 9, there is a sharp decrease in OCV when SOC is between 0 and 5%. A slight disturbance in voltage measurement can lead to significant inaccuracy. In fact, the OCV curves for li-ion cells always have a large plateau, and thus voltage-based SOC estimation works particularly poorly on li-ion cells.

Nevertheless, this method is still worth mentioning. The OCV curve is crucial for other estimation methods, and this method gives us an idea of how to obtain this curve for a particular cell in the test. In short, the cell is charged/discharged at a very small current (C/30) and is assumed to be resting. In this way, the OCV relationship can be obtained.
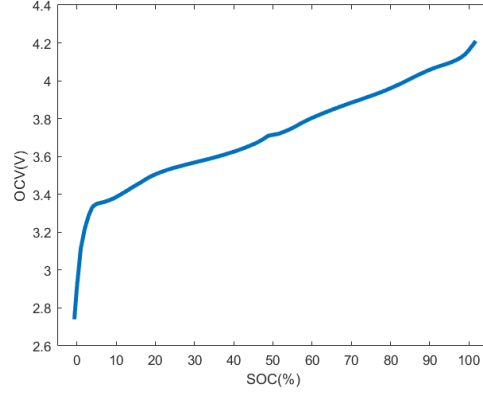
Figure 9: SOC versus OCV lookup table

Section 3.4 will provide a more detailed insight into this.

4.2.2 Coulomb counting

To use current as the primary estimator of SOC, recall the definition of SOC in Eq. (4.3) and rewrite it into

$$z_{k+1} = z_0 - \frac{\Delta t}{Q} \sum_{j=0}^{k-1} \eta_j i_j$$

where z_0 is the initial SOC. This is a precise method to estimate SOC, where the main challenges lie in the precise measurement of the current, the precise estimates of the coulombic efficiency η as well as the total capacity. The method is called *coulomb counting*. If we take a closer look into the current, it comprises several components:

$$i_j = i_{\text{true},j} + i_{\text{noise},j} + i_{\text{bias},j} + i_{\text{nonlin},j} - i_{\text{self-discharge},j} - i_{\text{leakage},j}$$

In Eq. (4.2.2), only the true current term $i_{\text{true},j}$ represents the true value of the current while all other terms are errors that accumulate over time. The noise and nonlinear errors are assumed to have zero mean, and they would not affect the expected value of the SOC estimate. On the other hand, the bias, self-discharge, and leakage errors do not follow a normal distribution, and thus they will accumulate over time to degrade continually. Also, the uncertainty in the measurement error will lead to the growth of the SOC estimate.

Besides, the coulomb counting method requires a precise initial voltage measurement every time the algorithm starts working. However, this is not an easy task as the cell is not always at rest initially, and the OCV method cannot apply. One may propose using the SOC value from the last loop, but then self-discharge should be considered if the cell has been at rest for a long time. However, coulomb counting is still widely applied in

24

real-time systems as it is computationally efficient, simple, and relatively accurate.

4.2.3 Model-based method

Model-based methods use a cell model, voltage, and current measurements to estimate, e.g., Luenberger observer, adaptive filter, particle filter, and sliding mode observer. Inputs to the actual system are also fed into the proposed model to estimate unmeasurable internal states. Also, by comparing the output estimates and the output measurements, we can know whether or not the state estimate is accurate.

These methods are much more accurate and reliable than coulomb counting as some of them can cancel out the effect of noise. They are also widely applied in real-time systems as well. Nevertheless, they tend to be computationally intensive and require additional laboratory tests to identify model parameters at varying ambient conditions.

In this thesis, the extended Kalman filter (EKF) is of particular interest and will be discussed and implemented in Section 4.3.

4.2.4 Machine learning

Machine learning is a flexible and efficient approach for state estimation. Unlike the model-based method, it does not require prior knowledge of the physical model. That means no laboratory tests are needed to obtain the cell models. With data collected directly from working cells, machine learning algorithms can learn their parameters and return the fitting results. Table 6 summarizes approaches taken by various researchers over the past few years. Methods, input features, and performances are listed.

Neural networks are likely the industry-leading machine learning technique because of their relatively high accuracy compared to other machine learning methods. Hence, they are widely used for battery state estimation. It is the nature of a BESS that it has access to a large amount of data. The data can be collected in a small increment of time as the battery develops and the neural network works well on data-rich systems (Ng et al. 2020). In this thesis, recurrent neural network (RNN) with long short-term memory (LSTM) cells are applied for SOC estimation, see Section 4.4.

A support vector machine (SVM) is a generalization of the random forest where the functions trained are simultaneously classified in a multidimensional space rather than split along one input direction. For an SVM to find the deterministic function that defines the relationship between the independent variables and the dependent variables, it needs to minimize the objective function.

Antón et al. (2013), Hu & Jain (2015) and Hu et al. (2014) used a support vector machine to predict SOC of Li-ion batteries. With different feature selections, an absolute error of 12.2%, 2.1% ,and 0.6% are obtained, respectively.

Gaussian process is a stochastic method that delivers a probability distribution of possible predictions

$$p(y) = N(\mu(x), \sigma^2(x)) \tag{4.4}$$

where it denotes a normal distribution with mean $\mu(x)$ and variance $\sigma^2(x)$. When the

Table 6: Summary of recent work on machine learning for SOC estimation, adapted from Ng et al. (2020)

Ref.	Method			Feature set					Error
	ANN	SVM	Gaus.	Vol.	Cur.	Temp.	Cyc. num.	Cap.	(%)
Bermejo et al. (2018)	×			×	×	×			1.3
Sahinoglu et al. (2017)			×	×	×	×			0.8
Antón et al. (2013)		×		×	×	×			12.2
Tong et al. (2016)	×			×	×	×			3.8
Kang et al. (2014)	×			×	×			×	10
Hu et al. (2015)	×			×	×				1.7
Wu et al. (2012)	×			×	×	×			3
Hu & Jain (2015)		×	×	×	×			×	2.1
Hu et al. (2014)		×		×	×	×	×		0.2

model receives the input, it computes the joint probability distribution of the fitting functions and the training data. The capability of this method is similar to an actual normal distribution: when the predictions are close to known training data, the model is good at capturing such a similarity; when the predictions are further from the known knowledge, the model's uncertainty increases.

Sahinoglu et al. (2017) used Gaussian process regression to estimate the SOC of li-ion batteries. The model chooses voltage, current and temperature as inputs feature and the Gaussian processes are shown to estimate SOC within 0.8%.

When it comes to selecting the most appropriate machine learning algorithm, several factors need to be considered, such as the amount of data, the quality of desired results, and the physical interpretability of the model (Ng et al. 2020).

4.3 Extended Kalman filter

In this section, the EKF algorithm is first and foremost presented and discussed. Then, both the method to identify the cell model and the dataset used for this thesis are briefly introduced. Finally, the experiment results are presented and discussed.

This section on EKF theory is based on the works by Plett (2015*b*), Chapter 3. It is a common approach in practice and can work well if the system's nonlinearities are mild. The EKF is based on the following two assumptions:

1. When computing estimates of the output of a nonlinear function, the EKF assumes that the expected value of a nonlinear function of the unknown state is equal to the same nonlinear function evaluated at the expected value of the state.
2. When computing covariance estimates, the EKF uses a truncated Taylor-series expansion to linearize the system equations around the present operating point. Higher-order terms from the expansion are discarded. This is why the EKF works best for systems with only mild nonlinearities.

The nonlinear system representation is given as follows:

$$x_{k+1} = f(x_k, u_k, w_k) \tag{4.5}$$

$$y_k = h(x_k, u_k, v_k) \tag{4.6}$$

Here, x_k, u_k, and y_k denote states, inputs and output, respectively. Process noise w_k and measurement noise v_k are assumed to be uncorrelated white Gaussian noise, with zero mean and covariance matrices having the properties:

$$\mathbb{E}\left[w_n w_k^T\right] = \begin{cases} \Sigma_{\tilde{w}}, & n = k \\ 0, & n \neq k; \end{cases} \qquad \mathbb{E}\left[v_n v_k^T\right] = \begin{cases} \Sigma_{\tilde{v}}, & n = k \\ 0, & n \neq k \end{cases} \tag{4.7}$$

The EKF comprises two main steps: prediction and correction. Each step consists of three sub-steps.

Prediction step 1 - Priori state prediction update.
Using EKF assumption 1, the state prediction step is approximated as

$$\hat{x}_k^- \approx f\left(\hat{x}_{k-1}^+, u_{k-1}, \bar{w}_{k-1}\right) \tag{4.8}$$

we approximate the expected value of the new state by assuming that it is reasonable to propagate $\hat{x}_{k-1}^+$ and $\bar{w}_{k-1}^-$ through the state equation.

Prediction step 2 - Priori error covariance update.
The covariance-prediction step is accomplished by first making an approximation for $\tilde{x}_k^-$:

$$\tilde{x}_k^- = x_k - \hat{x}_k^-$$
$$= f\left(x_{k-1}, u_{k-1}, w_{k-1}\right) - f\left(\hat{x}_{k-1}^+, u_{k-1}, \bar{w}_{k-1}\right) \tag{4.9}$$
$$\approx \hat{A}_{k-1}\tilde{x}_{k-1}^+ + \hat{B}_{k-1}\tilde{w}_{k-1}$$

Then we can find the prediction-error covariance:

$$\Sigma_{\tilde{x}_k}^- = \hat{A}_{k-1}\Sigma_{\tilde{x},k-1}^+\hat{A}_{k-1}^T + \hat{B}_{k-1}\Sigma_{\tilde{w}}\hat{B}_{k-1}^T \tag{4.10}$$

Prediction step 3 - System output prediction.

Using EKF assumption 1, the system output is approximated by

$$\hat{y}_k \approx h\left(\hat{x}_k^-, u_k, \bar{v}_k\right) \tag{4.11}$$

We approximate the expected value of the output by assuming that it is reasonable simply to propagate the state prediction $\hat{x}_k^-$ and the mean sensor noise $\bar{v}_k$ through the output equation.

Correction step 1 - Kalman gain update
The output prediction error can be written as

$$\begin{aligned}
\tilde{y}_k &= y_k - \hat{y}_k \\
&= h\left(x_k, u_k, v_k\right) - h\left(\hat{x}_k^-, u_k, \bar{v}_k\right) \\
&\approx \hat{C}_k \tilde{x}_k^- + \hat{D}_k \tilde{v}_k
\end{aligned} \tag{4.12}$$

As the total derivatives are equal to the partial derivatives, we can compute the following terms:

$$\Sigma_{\tilde{y},k} \approx \hat{C}_k \Sigma_{\tilde{x},k}^- \hat{C}_k^T + \hat{D}_k \Sigma_{\tilde{v}} \hat{D}_k^T \tag{4.13}$$

And the Kalman gain is computed with

$$L_k = \Sigma_{\tilde{x},k}^- \hat{C}_k^T \left[\hat{C}_k \Sigma_{\tilde{x},k}^- \hat{C}_k^T + \hat{D}_k \Sigma_{\tilde{v}} \hat{D}_k^T\right]^{-1} \tag{4.14}$$

Correction step 2 - Posteriori state estimate measurement update
This step computes the state estimate by updating the state prediction using the estimator gain and $y_k - \hat{y}_k$.

$$\hat{x}_k^+ = \hat{x}_k^- + L_k\left(y_k - \hat{y}_k\right) \tag{4.15}$$

Correction step 3 - Posteriori error covariance measurement update
Finally, the updated covariance is computed as

$$\Sigma_{\tilde{x},k}^+ = \Sigma_{\tilde{x},k}^- - L_k \Sigma_{\tilde{y},k} L_k^T \tag{4.16}$$

For the ECM proposed in Chapter 3, the $\hat{A}_k$, $\hat{B}_k$, $\hat{C}_k$, $\hat{D}_k$ matrices are computed analyti-

cally from the Jacobian of the system representation

$$\hat{A}_k = \frac{\partial}{\partial \mathbf{x}_k} \mathbf{f}(\mathbf{x_k}, \mathbf{u_k}, \mathbf{w}_k) = \begin{bmatrix} 1 & 0 \\ 0 & A_{RC} \end{bmatrix} \tag{4.17}$$

$$\hat{B}_k = \frac{\partial}{\partial \mathbf{w}_k} \mathbf{f}(\mathbf{x_k}, \mathbf{u_k}, \mathbf{w}_k) = \begin{bmatrix} -\frac{\eta_k \Delta t}{Q} \\ 1 - A_{RC} \end{bmatrix} \tag{4.18}$$

$$\hat{C}_k = \frac{\partial}{\partial \mathbf{x}_k} \mathbf{h}(\mathbf{x_k}, \mathbf{u_k}, \mathbf{v}_k) = \begin{bmatrix} \frac{\partial OCV(z_k)}{z_k} & -R_1 \end{bmatrix} \tag{4.19}$$

$$\hat{D}_k = \frac{\partial}{\partial \mathbf{v}_k} \mathbf{h}(\mathbf{x_k}, \mathbf{u_k}, \mathbf{v}_k) = -R_0 \tag{4.20}$$

4.4 Recurrent neural network (RNN) with long short-term memory (LSTM) cells for SOC estimation

Long short-term memory (LSTM) is a recurrent neural network (RNN) architecture used in natural language processing, speech recognition, and time series analysis. The input/output data of a battery cell also belong to time series, and thus, time series analysis approaches can be applied. In this thesis, we adopted RNN with an LSTM cell for SOC estimation. Chemali et al. (2018) summarizes the following strengths of a LSTM-RNN model compared to the EKF:

- The LSTM-RNN can map measurements (voltage, current, and temperature) directly to the SOC. Compared to adaptive filters, it takes less computational efforts.
- To establish a battery model for EKF, multiple laboratory tests are required, as introduced in Chapter 3. Also, the tests are only valid for a specific temperature. For various ambient temperatures, different tests should be performed. The LSTM-RNN model can learn its network parameters by being fed training data, which the BMS can easily obtain from practice in a short time duration. When temperature is an input feature, one LSTM-RNN can learn to estimate SOC throughout various different ambient temperature conditions.

4.4.1 RNN and LSTM

Traditional neural networks cannot capture the dependencies between time steps in time series. However, by Eq. (4.3), the current has an accumulative effect on the cell SOC. Neural networks with no memory functions are not ideal in this regard. As shown in Fig. 10, where x_k, y_k are the inputs and outputs, the loops in the RNN architecture enable information to be passed from one step to the next. If the RNN is unrolled, it can be thought of as multiple copies of the same network, each passing the information to a successor. This chain-like nature reveals that RNNs are closely related to sequences,
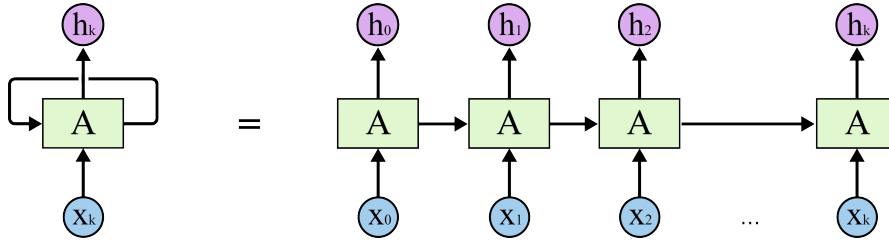
Figure 10: RNN architecture (Olah 2015)

which means they are suitable for SOC estimation.

However, the typical RNN suffers from short-term memory. If an input sequence is too long, the network will not be able to carry information from earlier time steps to later ones. In other words, RNN is not capable of learning long-term dependencies. Proposed by Hochreiter & Schmidhuber (1997), the LSTM aims to solve this problem.
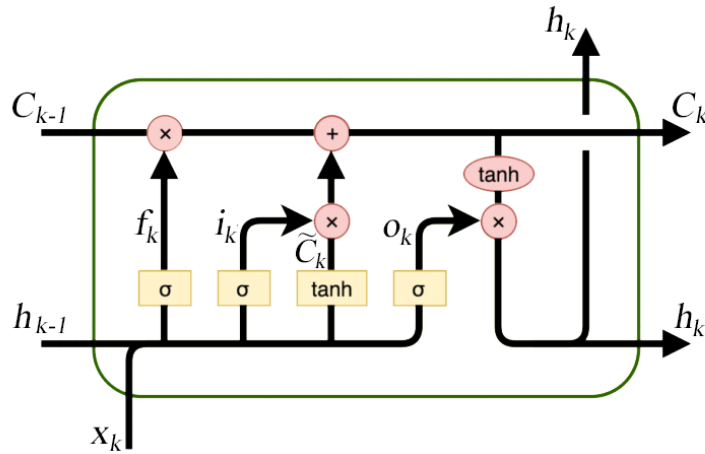
Figure 11: LSTM node (Olah 2015)

Fig. 11 shows the structure of a LSTM cell. It comprises three gates: forget gate, input gate, and output gate. The forget gate decides what information to discard and what to leave. It looks at h_{k-1} and x_k, and returns a number between 0 and 1 with the sigmoid function $\sigma(x) = (1 + e^{-x})^{-1}$. A one represents "completely keep this" and a zero represents "completely discard this". The function is written as

$$f_k = \sigma(W_{xf}x_k + W_{hf}h_{k-1} + b_f) \tag{4.21}$$

Here, W_{xf} and W_{hf} denote the weights for the gate. A bias term b_f is added at the gate to increase the network's flexibility to fit the data.

The input gate layer decides which values we will update. Next, a tanh layer creates

a vector of new candidate values, $\tilde{C}_k$, that could be added to the state. In the next step, we will combine these two to create an update to the state.

$$i_k = \sigma\left(W_{xi}x_k + W_{hi}h_{k-1} + b_i\right) \tag{4.22}$$

$$\tilde{C}_k = \tanh\left(W_{xC}x_k W_{hC}h_{k-1} + b_C\right) \tag{4.23}$$

The current state C_k is updated based on the previous state C_{k-1} and the new candidate value $\tilde{C}_k$.

$$C_k = f_k C_{k-1} + i_k \tilde{C}_k \tag{4.24}$$

Finally, the output gate decides what it is going to output. The sigmoid function decides which parts of the cell state to output, and the cell state is passed through tanh and multiplied by the output.

$$o_k = \sigma(W_{xo}x_k + W_{ho}h_{k-1} + b_o) \tag{4.25}$$

$$h_k = o_k \tanh(C_k) \tag{4.26}$$

4.4.2 Data pre-processing

In this thesis, we only use the ten drive cycles at 25°C for SOC estimation. As opposed to the traditional method that divides the entire dataset into, e.g., training set: validation set: test set = 0.7:0.15:0.15, the network is trained by feeding one drive cycle at a time. Specifically, seven drive cycles (US06, NN, HWFT, and mixed cycles 1-4) are used as the training set, while one drive cycle (UDDS) is used as the validation set and one drive cycle (LA92) as the test set. This method is commonly performed for training RNN models, as the consistency of a sequence is of vital importance. Each drive cycle has a length of over 100 000 time steps, and a personal laptop cannot process such a massive amount of data. This is why not all ten cycles are used in the experiment.

Furthermore, the data are standardized to have a zero-mean and a variance of one. It is done by:

$$x' = \frac{x - \mu}{\sigma} \tag{4.27}$$

where μ is the mean value of the data and σ is the variance. It helps to accelerate the convergence speed.

4.4.3 Implementation

In this thesis, the *Deep Learning Toolbox* on MATLAB is used in conjunction with a GeForce GTX 1050Ti graphics card on a personal laptop. Limited by the performance

of the graphics card, a high number of hidden units is not permitted, and thus the performance of the networks may not be optimal.

Fig. 12 illustrates the architecture of a LSTM-RNN for regression. The network comprises three layers: the input layer, the LSTM layer, and the output layer. The input layer receives sequential data and feeds them to the LSTM layer. The output layer receives fitting results from the LSTM layer and feeds back the error to start a new training epoch.
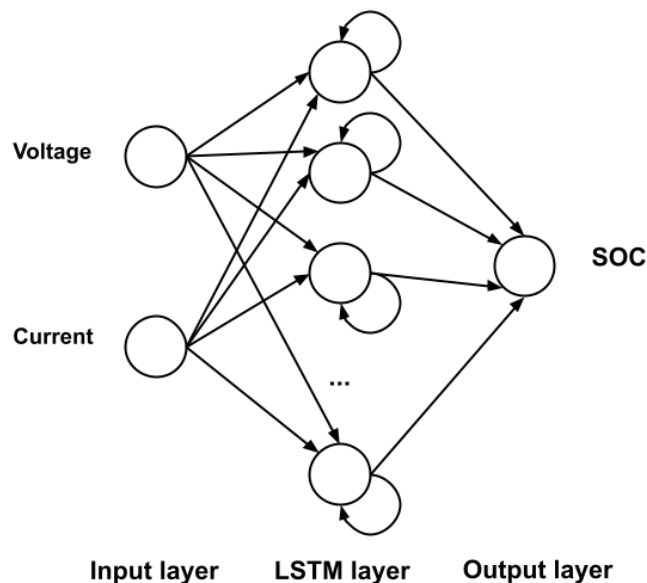
Figure 12: LSTM-RNN topology for SOC estimation

The sequence input layer takes the input sequence with the specified number of features, which is 2 (voltage and current) in this thesis. The LSTM outputs the hidden state and the cell state. As we want the output SOC to be a sequence instead of just one value, we should set the output mode of the LSTM layer to 'sequence'. The output layer performs a linear transformation on the hidden state h_k to obtain a single estimated SOC value at time step k. This is done as follows:

$$z_k = W_{out}h_k + b_y \tag{4.28}$$

where W_{out} and b_y are the fully connected layer's weight matrix and bias, respectively.

4.4.4 Networks training

When the data are ready, we can start training our networks. As we only use data at 25°C, the temperature is not used as an input feature. The objective is to estimate SOC based on the input sequence of voltage and current. The hyperparameters that need to be tuned include

- the maximum epochs,
- the minimum batch size,
- the initial learning rate,
- the number of hidden layers, and
- the L2 regularization rate.

It is easy to determine the maximum epochs as the performance of the networks does not improve significantly after a certain number of epochs, which in this case, around 80. The minimum batch size decides how "efficient" the program will be, and a larger minimum batch size enables the networks to process more data simultaneously. A common choice for it will be 32, 64, or 128. A high initial learning rate would allow the networks to converge faster, but at the same time, it may be difficult for the networks to find the optimal parameters to minimize the cost function. One alternative would be using a piecewise learning rate schedule, where the learning rate drops by, e.g., 0.1 time after 50 epochs. It ensures the networks can converge quickly at the beginning of the training and that the optimal solutions can be found towards the end.

The number of hidden nodes directly determines the performance of the networks, the computational complexity, and the training time. A higher number of hidden nodes increase the complexity of the networks, but it does not necessarily mean the performance will improve simultaneously. The networks may encounter an overfitting problem once the number of hidden nodes is too high, while a number of hidden nodes that is too low will result in underfitting. At the same time, L2 regularization prevents overfitting, while it would also lead to underfitting when the L2 regularization is too high. Therefore, it is tricky to find the proper hyperparameters for the networks.

One efficient way to tune the hyperparameters is using the validation set as an indicator. During the training process, the networks act on the validation set and return the errors on the training set and the validation set. If the validation error deviates a lot from the training error, the networks are overfitting/underfitting. The advantage of using a validation set is that we do not have to wait until the entire training process ends, and we can know the performance of the networks as the training is in the process.

4.5 Results and discussion

4.5.1 Matrics

The following three matrics are used to evaluate the models throughout the thesis.

Mean absolute error (MAE)

The MAE is defined as

$$\text{MAE} = \frac{1}{n} \sum_{i=1}^{n} \frac{|y_i - \hat{y}_i|}{y_i} \times 100 \tag{4.29}$$

where y_i is the measurements, $\hat{y}_i$ is the estimates, and n represents the total number of samples.

Root mean square error (RMSE)

With the same scale as MAE, the RMSE reflects the deviation in errors. It is defined as

$$\text{RMSE} = \frac{1}{n} \sum_{i=1}^{n} |y_i - \hat{y}_i|^2 \tag{4.30}$$

Coefficient of determination (R^2)

R^2 measures how well the model explains the observed variability in the target variable. R^2 ranges from 0 to 1 where a value of 1 indicates the model can explain all the variabilities of the target class. It is given as

$$R^2 = 1 - \frac{\sum_{i=1}^{n}(y_i - \hat{y}_i)^2}{\sum_{i=1}^{n}(y_i - \bar{y})^2} \tag{4.31}$$

where $\bar{y}$ represents the mean of measurements.

4.5.2 EKF results

With the OCV relationship and the model parameters determined in Section 3.4, we can start implementing the EKF. The EKF implementation is based on the ESC toolbox from Plett (2015*a*). Before entering the main loop, an initialization step is required to load the cell model and the drive cycle data, and to create initial states and initial covariance values. The covariance values are the tuning parameters that have a great effect on the results. After initialization complete, we enter the main program loop. It takes voltage, current, and temperature as inputs, executes the EKF algorithm step by step, and returns the SOC estimate as well as the output estimate at the current time step.

Fig. 13 shows the LA92 drive cycle used for testing the EKF. The cell began in a fully charged state and completed the drive cycle test at around 5% SOC, and the ambient temperature is 25°C.

Fig. 14(a) compares the estimate by the EKF and the measurement, and Fig. 14(b) shows the estimation error over time. The estimation MAE is 0.27%, and the RMSE is 0.52%. The error is outside of error bounds 5.0% of the time, and it occurs at the beginning of the process. It can be seen from the figures that the EKF has an good capability of tracking the actual SOC within an acceptable error bound.

The EKF is further performed on nine drive cycles at an ambient temperature of 25°C.

34

(a) Voltage measurements

(b) Current profile

(c) Capacity
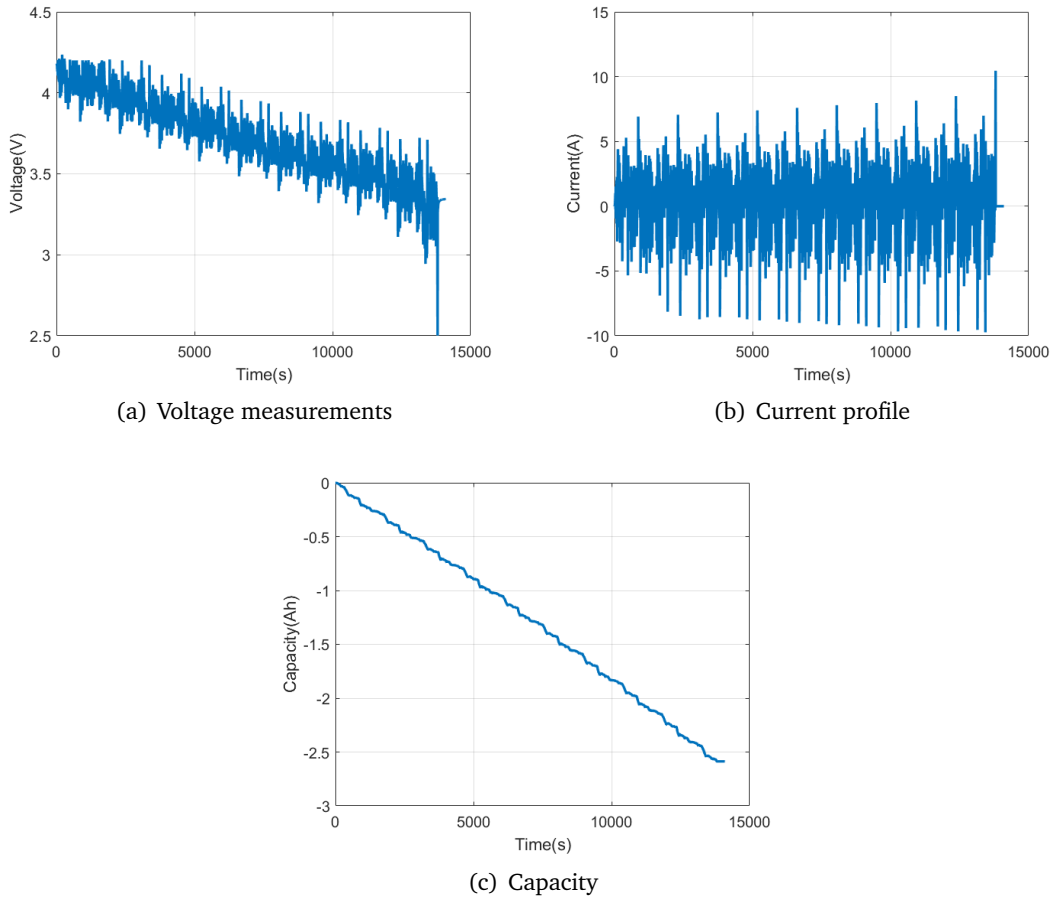
Figure 13: LA92 drive cycle recorded at an ambient temperature of 25°C

Table 7 summarizes the MAE and RMSE for each drive cycle, and the average MAE and RMSE are 0.64% and 0.77%, respectively.

Table 7: EKF performance for nine drive cycles

Drive Cycle	MAE (%)	RMSE (%)	Drive Cycle	MAE (%)	RMSE (%)
LA92	0.27	0.52	HWFTb	0.61	0.78
US06	1.14	1.07	Mixed cycle 1	0.19	0.44
UDDS	0.29	0.54	Mixed cycle 2	0.88	0.94
NN	0.45	0.67	Mixed cycle 3	0.76	0.87
HWFTa	1.18	1.09	Average	0.64	0.77

Although the EKF gives a satisfying estimation result, there are still flaws with this

(a) SOC estimation using EKF   (b) SOC estimation error using EKF

Figure 14: EKF performance for LA92 drive cycle

method compared to machine learning. It takes extra laboratory work to collect data for system identification, while machine le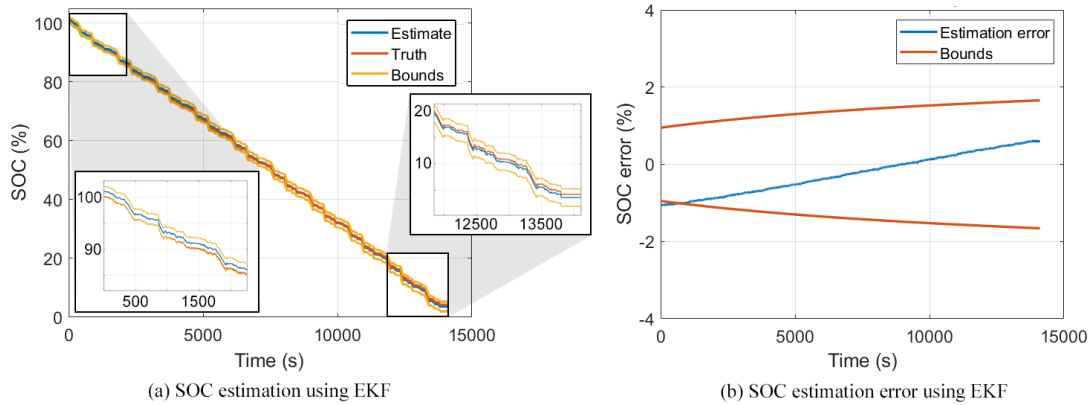arning can map the voltage, current, and temperature directly to SOC. Also, the tuning of parameters takes a considerable amount of time, and they significantly impact the performance. Machine learning also requires tuning, but the process is relatively easy as only the hyperparameters need to be tuned.

Nevertheless, EKF is still a commonly applied state estimation method for nonlinear systems. Chpater 5 power limit estimation and Chapter 7 fault detection are based on the EKF developed in this chapter.

4.5.3 LSTM-RNN results

The learning curve, which indicates the performance of the training process, is shown in Fig. 15. The figure shows that the overall error and loss are low, and the validation error matches the training error. This proves that the networks have an excellent ability to estimate SOC without overfitting/underfitting.

After the training process is finished, we use the test set data (LA92 drive cycle) to test the performance of the networks. Fig. 16(a) shows the SOC estimates by LSTM-RNN and by EKF, as well as the measurement values. Fig. 16(b) shows the error using LSTM-RNN over all time steps. The MAE of LSTM-RNN is 0.84%, and the RMSE is 1.0%. Both EKF and LSTM-RNN give a satisfying performance in estimating SOC. However, if we take a closer look at the curve, we can find that although the EKF can track the measurement value better than LSTM-RNN, its output keeps a static error at all times.

Given that a BESS can obtain a considerable amount of data, the machine learning method seems natural for SOC estimation. The LSTM-RNN model provides a competitive performance compared to EKF, and by its nature, it is a very suitable method in the machine learning family. Also, in traditional techniques like KF, the model parameters must be identified via laboratory experiments, and the covariance matrices need to be determined. The LSTM-RNN model can learn the network parameters with actual operating data, freeing engineers from tuning the models themselves. Overall, this section
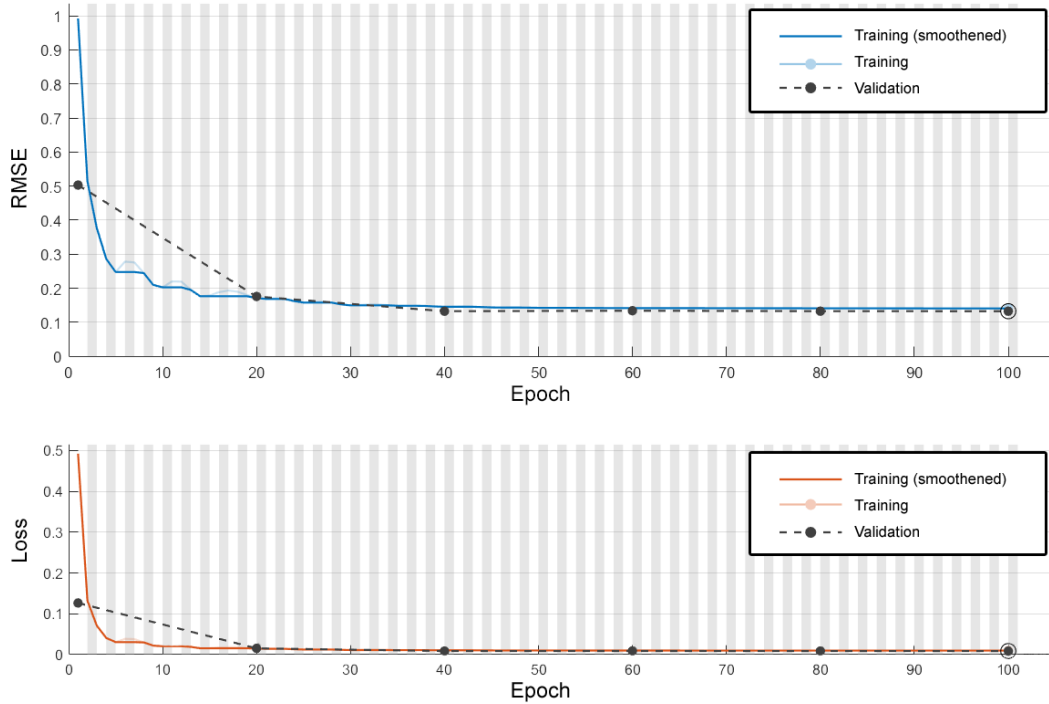
36

Figure 15: The learning curve for the LSTM-RNN model

showcases the theory behind the LSTM-RNN model and its competitive performance on actual data compared to EKF.

Nevertheless, there are still several unanswered questions in this thesis:

- The effect of temperature is not considered during the system identification process and the network training. The algorithms are only performed at 25°C, and therefore, further study can focus on building battery models and training the networks at various temperatures.
- The amount of data is not enough to consider cell aging and degradation. Usually, a Li-ion battery has a cycle life from 500 to 1000, while the cycles provided in the dataset are independent and short. In other words, this dataset is not suitable for SOH estimation.
- The dataset used in this chapter is not for marine applications. Compared to batteries in an EV, batteries on a vessel or an ROV have a higher C-rate to handle the complex environment, and their performance will be different. Unfortunately, up to date, there is not public dataset for marine Li-ion batteries.

4.6   Summary

In this chapter, we first introduce the definition of SOC and the ECM of battery cells. Then, four methods for SOC estimation are presented, and the Kalman filter and ma-

(a) SOC estimation with LSTM-RNN   (b) SOC estimation error with LSTM-RNN
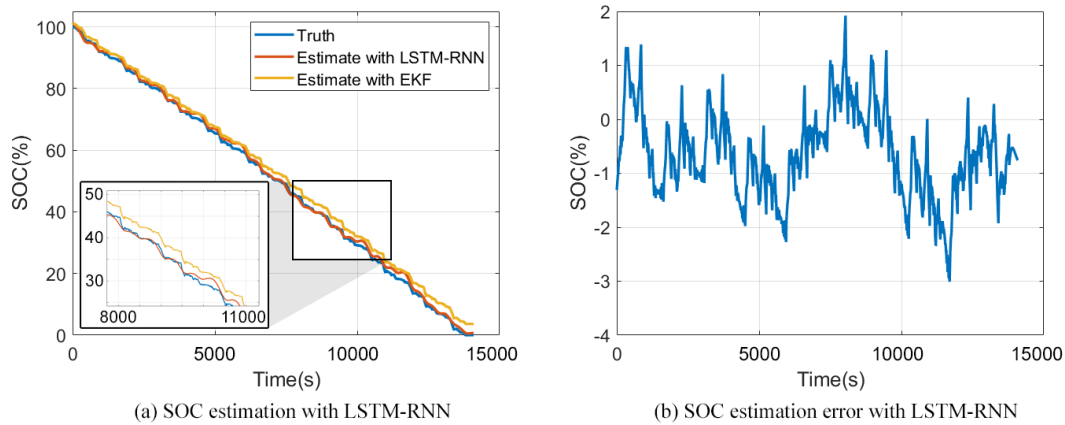
Figure 16: LSTM-RNN performance for SOC estimation

chine learning become the main focuses in this chapter. For the Kalman filter, it is essential to perform two tests to identify the battery cell model. The performance of the Kalman filter on the Panasonic 18650PF dataset shows an MAE of 0.32% and an RMSE of 0.56%. An LSTM-RNN model is also implemented and tested on the same dataset, giving an MAE of 0.84% and an RMSE of 1.01%. Further experiments, using temperature as an input feature, could shed more light on the effect of temperature on SOC estimation.

Chapter 5

Power Limit Estimation

A power limit contains information about how quickly energy can be added to or removed from the battery pack without violating a set of design constraints (Plett 2015*b*). A power output that is too low for a battery pack will decrease its performance, while a power output that is too high will accelerate its aging. Therefore, there exists a trade-off between the performance and the expected lifetime. To compute the power limit is essentially to optimize this trade-off.

One common way to impose these constraints is by limiting the terminal voltage, as the BMS can obtain it directly. The other is to include SOC-based limits in addition to the voltage-based limits. This chapter will focus on how to calculate the power limit using two different methods.

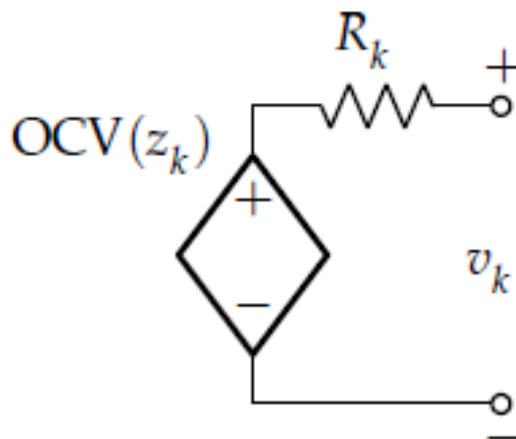## 5.1 Hybrid pulse power characterization (HPPC) using a simplified model

Figure 17: Simplified battery model from Plett (2015*b*)

Section 5.1 and 5.2 are based on the work of Plett (2015*b*) and Frankforter et al. (2020). HPPC is a standard method to estimate power limits. This method uses a simplified model, as shown in Fig. 17. The terminal voltage can be expressed as

$$v_k = OCV(z_k) - i_k R_k \qquad (5.1)$$

By rearranging the terms we have

$$i_k = \frac{OCV(z_k) - v_k}{R_k} \qquad (5.2)$$

If we constrain the voltage to its minimum design voltage v_{min}, the discharge power is then expressed as

$$p_{dis,k} = v_k i_k = v_{min} \frac{OCV(z_k) - v_{min}}{R_k} \qquad (5.3)$$

The R_k is essentially the equivalent series resistance R_0. However, if we want to find the maximum discharge power, it is crucial to model a larger R_k value. The HPPC method aims at finding the R_k by applying pulses.
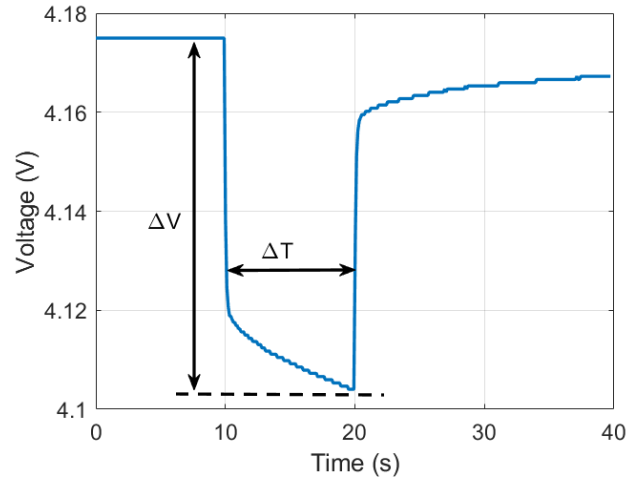
Figure 18: HPPC voltage

As shown in Fig. 18, a constant current pulse i_{dis} is applied to the cell for a duration of $\Delta T = 10s$, resulting in a decrease in the cell voltage Δv_{dis}. The cell stays at rest after the pulse and waits for the next to come. The discharge resistance over the $\Delta T = 10s$ duration is computed as:

$$R_{dis,\Delta T} = \left| \frac{\Delta v_{dis}}{i_{dis}} \right| \qquad (5.4)$$

So, by setting $R_k = R_{dis,\Delta T}$, we can compute the maximum discharge current and maximum discharge power as

$$i_{max,k}^{dis,volt} = \frac{OCV(z_k) - v_{min}}{R_{dis,\Delta T}} \tag{5.5}$$

$$p_{max,k}^{dis,volt} = v_{min} i_{max,k}^{dis,volt} \tag{5.6}$$

As the dataset from Chemali et al. (2018) contains HPPC tests at different temperatures, we will use this simple method to estimate maximum power in Section 5.3.

5.2   Enhanced HPPC using an ECM model

The performance of the HPPC method can be improved by using the ECM model proposed in Chapter 2. Depending on the constraints used, there are two different methods: voltage-based and SOC-based.

5.2.1   Voltage-based estimation

During operation, the BMS estimates the power limits and communicates to the load-management system. If the battery pack acts as the sole power source, such as in an all-electric ferry, the load controller must ensure that the power limits are not violated, even if it means a loss in performance. Suppose the battery pack is one of many power sources. In that case, the load controller uses the maximum limits from the battery management system as part of its strategy to blend the capabilities of the two sources intelligently to satisfy the load requirements while optimizing some performance criteria (Plett 2015*b*).

In applications, the power limit is not estimated at each time instant, as the true available power does not change rapidly. A slowly-varying power limit can avoid abrupt changes in the battery pack load. More importantly, instead of an instantaneous estimate, a predictive estimate of power is preferred so that the system can make a load plan over a near-future time horizon. Therefore, the estimate of power limit over the next ΔTs is of particular interest. At this point, one may notice that the power limit p_{max} is most likely provided by the manufacturer. However, we need to adopt a more conservative strategy to provide a power range for redundancy to absorb a short-term exceedance. That explains why the power limit should be estimated even though the maximum power is known.

However, the computation is done more frequently than every ΔTs. This approach is called *overlapping moving-window*. It acts as a low-pass filter and can smooth the estimates.

Before introducing the algorithm, the following notations and assumptions are required. We denote:

- Cell terminal voltage at time instant k by v_k; where design limits $v_{min} \leq v_k \leq v_{max}$

must be enforced;

- Cell current at time k, where $i_{min} \leq i_k \leq i_{max}$ is enforced;
- SOC at time k by z_k, where $z_{min} \leq z_k \leq z_{max}$ is enforced;
- Cell power at time k by p_k, where $p_{min} \leq p_k \leq p_{max}$ is enforced;

The HPPC method uses a simplified battery model with only an OCV and equivalent series resistance. To obtain higher accuracy, Plett (2015*b*) improved the method by including the diffusion voltage.

Now, recall the ECM in Chapter 2. Its discrete-time state-space model is

$$\begin{bmatrix} z_{k+1} \\ i_{R,k+1} \end{bmatrix} = \begin{bmatrix} 1 & 0 \\ 0 & A_{RC} \end{bmatrix} \begin{bmatrix} z_k \\ i_{R,k} \end{bmatrix} + \begin{bmatrix} -\frac{\eta_k \Delta t}{Q} \\ 1 - A_{RC} \end{bmatrix} i_k.$$

$$v_k = OCV(z_k) - R_1 i_{R_1,k} - R_0 i_k$$

The cell voltage ΔTs into the future can be expressed by

$$v_{k+\Delta T} = OCV(z_{k+\Delta T}) - R_1 i_{R_1,k+\Delta T} - R_0 i_{k+\Delta T} \tag{5.7}$$

where $OCV(z_{k+\Delta T}), R_1 i_{R_1,k+\Delta T}$ can be computed by the state function. In this case, the state function is linear. By assuming $i_k = i_{k+\Delta T}$, we have

$$x_{k+\Delta T} = A^{\Delta T} x_k + \left(\sum_{j=0}^{\Delta T-1} A^{\Delta T-1-j} \right) B i_k \tag{5.8}$$

The approach aims at finding two values: $i_{max,k}^{dis,\ volt}$, which represents the maximum discharge current at time instant k, using voltage-based method; and $i_{min,k}^{chg,volt}$, which represents the minimum charging current at time instant k, using the same method. $i_{min,k}^{chg,volt}$ is the numerical solution of i_k to the following equality:

$$v_{max} - v_{k+\Delta T} = 0 \tag{5.9}$$

Similarly, to compute $i_{max,k}^{dis,volt}$, we need to find an i_k such that the following equality is satisfied:

$$v_{min} - v_{k+\Delta T} = 0 \tag{5.10}$$

where v_{min}, v_{max} are provided by the manufacturer.

5.2.2 SOC-based power limit estimation

Cell SOC is another alternative to estimate power limit. The SOC into the future ΔTs is

$$z_{k+\Delta T} = z_k - \frac{\eta_k \Delta T}{Q} i_k \tag{5.11}$$

By rearranging the terms, we have

$$i_k = \frac{z_k - z_{k+\Delta T}}{\eta_k \Delta T / Q} \tag{5.12}$$

Thus, by enforcing the SOC constraints $z_{min} \leq z_k \leq z_{max}$, the current constraints are computed as

$$i_{max,k}^{dis,soc} = \frac{z_k - z_{min}}{\Delta T / Q} \tag{5.13}$$

$$i_{min,k}^{chg,\,soc} = \frac{z_k - z_{max}}{\eta \Delta T / Q} \tag{5.14}$$

where the coulomb efficiency $\eta_k = 1$ during discharging and $\eta_k \leq 1$ when charging.

However, the SOC estimates always come with errors, and a more conservative power limit estimate can be made by considering the errors. When using EKF, the confidence interval of SOC estimation at time instant k is denoted by $\sigma_{z,k}$. A $3\sigma_{z,k}$ confidence interval is assumed to be sufficient to include the true SOC estimate. Thus Eq. (5.13) and (5.14) can be modified as

$$i_{max,k}^{dis,soc} = \frac{(z_k - 3\sigma_{z,k}) - z_{min}}{\Delta T / Q} \tag{5.15}$$

$$i_{min,k}^{chg,soc} = \frac{(z_k - 3\sigma_{z,k}) - z_{max}}{\eta \Delta T / Q} \tag{5.16}$$

Once we obtain the cell current limits, we use the maximum/minimum value to compute the power limit:

$$i_{min,k}^{chg} = \max \left(i_{min}, i_{min,k}^{chg,volt}, i_{min,k}^{chg,soc} \right) \tag{5.17}$$

$$i_{max,k}^{dis} = \min \left(i_{max}, i_{max,k}^{dis,volt}, i_{max,k}^{dis,soc} \right) \tag{5.18}$$

The charge and discharge power can be computed as

$$p_{min,k}^{chg} = \max\left(p_{min}, i_{min,k}^{chg} v_{k+\Delta T}\right) \tag{5.19}$$

$$p_{max,k}^{dis} = \min\left(p_{max}, i_{max,k}^{dis} v_{k+\Delta T}\right) \tag{5.20}$$

To compute the power limit of a battery back, assume it comprises $N_s \geq 1$ cells connected in series and $N_p \geq 1$ cells in parallel. Eq. (5.19) and (5.20) can be modified as

$$p_{min,k}^{chg} = N_p \max\left(N_s p_{min}, \sum_{i=1}^{N_s} i_{min,k}^{chg} v_{k+\Delta T}^{(i)}\right) \tag{5.21}$$

$$p_{max,k}^{dis} = N_p \min\left(N_s p_{max}, \sum_{i=1}^{N_s} i_{max,k}^{dis} v_{k+\Delta T}^{(i)}\right) \tag{5.22}$$

5.3 Results and discussion

The proposed power limit design methods are tested with the short-term drive cycle performance dataset from Chemali et al. (2018). For the Panasonic 18650PF cell used in the test, the operational limits for voltage, current, SOC and power are summarized in Table 8. The tests are performed on a cell level as the dataset lacks data for an entire battery pack.

Table 8: Operational limits

	Minimum	Maximum
Voltage	2.5V	4.2V
Current	-30A	30A
SOC	10%	90%
Power	$-\infty$	$+\infty$

5.3.1 HPPC test

The HPPC data at 25°C is applied in the test. With Eq. (5.4), the average value for the discharge resistance is $R_{dis,\Delta T} = 38m\Omega$. Fig. 19(a) shows the design current limit. In the first 875min, the rated current is lower than the designed current limit and restricts the maximum power to $30A \times 2.5V = 75W$, as shown in Fig. 19(b). Subsequently, the designed current limit takes over, and the power limit starts varying according to it. The power profile throughout the test is lower than the power limit.
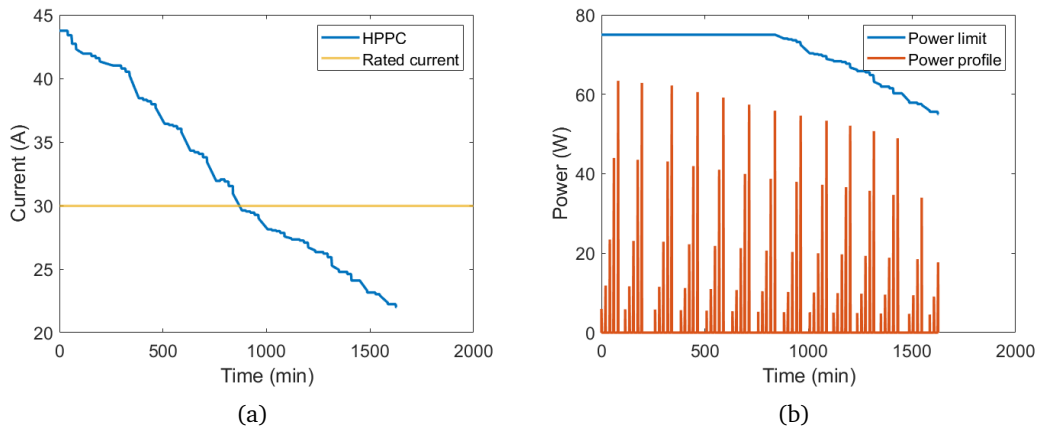
Figure 19: Power limit design using HPPC method

5.3.2 Enhanced HPPC test
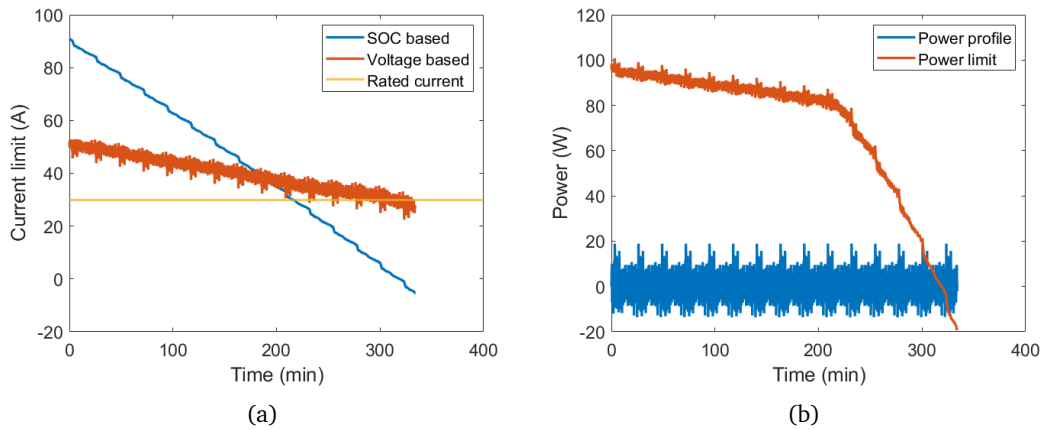
Figure 20: Power limit design using enhanced HPPC method

The UDDS drive cycle at 25°C is applied in the test. Instead of using the bisection method to predict the maximum discharge current in Eq. (5.10), the states are first computed with the EKF to simplify the process. The maximum current are shown in Fig. 20(a), where the rated current is dominant in the first 230min. Subsequently, the SOC-based maximum current takes over and the maximum power varies according to it. The voltage-based maximum current contains noise, resulting from the noisy voltage measurements.

Fig. 20(b) compares the power limit with the actual power profile. After around 300min, the power limit is lower than the actual power. For a BMS, a power control

strategy should be applied to reduce the power so that the operational safety can be ensured.

5.4 Summary

Enforcing power limits to the battery cells ensures safe operations. In this chapter, section 5.1 introduced a standard method - HPPC - for power limits design. The HPPC method is simple and straightforward, using a simplified battery model. Section 5.2 proposed the enhanced HPPC method by including the ECM model presented in Chapter 2. Based on the constraints used, the enhanced HPPC method can be further classified into voltage-based and SOC-based. Section 5.3 implemented the algorithms and presented the test results using the EKF and the dataset in Chapter 4. In summary, the HPPC method provides a systematic approach to optimize the tradeoff between the battery performance and life.

Chapter 6

State-of-Health Estimation and Remaining Useful Life Prediction

Batteries in a BESS age and degrade over time due to undesired side reactions in the cells. They will eventually reach a point where they no longer meet the performance requirements of the battery, which is considered the end of life (EOL) of the battery. Between a battery's beginning of life and EOL, it is crucial to have knowledge regarding the present degradation status of its cells. The state-of-health (SOH) estimation, also known as *health diagnosis*, is the key to evaluate the present degradation.

The EOL of a battery is also referred to as failure. We usually want to replace the battery for applications before failure occurs, as battery failure could result in degraded capability, unavailable operation, downtime, and even a catastrophic occurrence. The remaining useful life (RUL) prediction, also know as *failure prognosis*, is the key to predict battery failure. It requires the knowledge of the current and historical data, often obtained from the SOH estimator, to forecast the system's future state under certain operating conditions.

In this chapter, the indicators of battery degradation are presented in Section 6.1, as the degradation mechanisms will help us understand the diagnosis and prognosis process. Section 4.2 shows the mainstream methods for both SOH estimation and RUL prediction. Section 6.3 applies LSTM-RNN for SOH estimation and RUL prediction.

6.1 Battery degradation indicators

Total capacity and ESR can represent the degree of degradation of a battery cell. Typically, a cell is considered at EOL when its total capacity decreases below 80% of its nominal capacity or when its ESR doubles (Li et al. 2019). We will use these two indicators throughout the chapter, and a deeper understanding will help us how SOH and RUL are evaluated. The following discussion is adapted from Plett (2015*b*) and Tran & Fowler (2020).
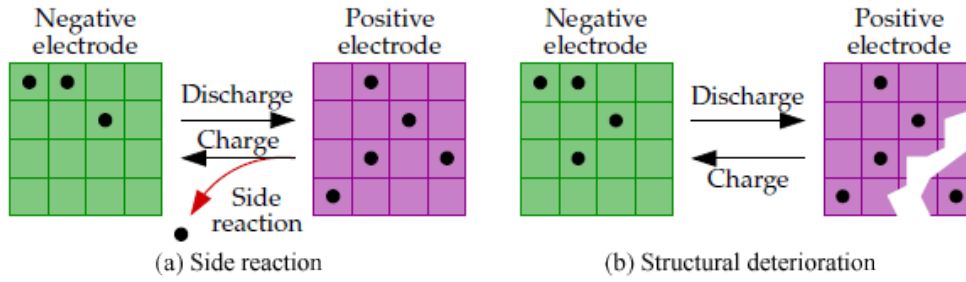
(a) Side reaction   (b) Structural deterioration

Figure 21: Two major factors that lead to degradation (Plett 2015*b*)

6.1.1 Total capacity Q

A battery cell's total capacity decreases as it ages. For a Li-ion cell, two common factors lead to degradation: undesired side reactions and structural deterioration.

The undesired side reactions consume lithium when the lithium transits from one electrode to another. The consumed lithium is permanently removed from the cycle, and thus the capacity decreases. Most side reactions occur during the charging process.

Structural deterioration of the electrode's active materials also leads to degradation. It eliminates lithium storage sites from one of the electrodes. A common cause that leads to structural deterioration is a collapse of part of the crystal structure of the electrode.

Although there is no universally agreed-upon definition of SOH, in this chapter, we define SOH using the total capacity as follows:

$$\text{SOH} = \frac{Q}{Q_{\text{nom}}} \times 100\% \tag{6.1}$$

where Q represents the total capacity of the cell at its current state and Q_{nom} is the nominal capacity which the manufacturer provides. Here, SOH is defined as a percentage. A fresh battery is at 100% SOH, and 80% SOH indicates the EOL of the battery.

An accurate total capacity estimation is essential for SOC estimation when using Coulomb counting. However, when using the Kalman filter, the SOC estimation is insensitive to a poor total capacity estimate. The built-in feedback correction mechanism is able to compensate for moderate errors in the total capacity estimate. This is another advantage of using the Kalman filter.

6.1.2 Equivalent series resistance (ESR) R_0

A battery cell's equivalent equivalent series resistance (ESR) as it ages. A high value of ESR will lead to degraded capability and hazards such as overheating. Here as well, the primary reasons are undesired side reactions and structural deterioration. The side reactions form resistive films on the surface of the active material particles that impede the ionic conductivity. Structural deterioration cuts off the electronic pathways between

particles and decreases the electronic conductivity.

An accurate estimation of the ESR is essential for SOC estimation using voltage-based methods. However, similar to the total capacity, the Kalman filter can compensate for moderate errors in the ESR estimate. For Coulomb counting, it does not have any effect.

6.2 Methods for SOH estimation and RUL prediction

Over the years, various SOH estimation and RUL prediction methods have been developed. Direct measuring methods include electrochemical impedance spectroscopy (EIS) and hybrid pulse power characterization (HPPC). However, these methods are only suitable in laboratories. For in-situ applications, one common idea is to simulate the behaviors of cells based on cell models. Model-based methods, such as the Kalman filter and particle filter, estimate the degradation indicators and SOH states. Aside from the ECM model, electrochemical models are also used to study battery degradation.

Data-driven methods for health diagnosis and failure prognosis are becoming the main focuses in recent years. Their advantages include flexibility and not requiring a model. However, the acquisition of high-quality data in various operating conditions still remains a problem.

6.2.1 Model-based methods

The Kalman filter is a universal method for both state and parameter estimation. In Chapter 4, we implemented an EKF to estimate SOC, while in fact, we can modify the EKF to estimate battery parameters such as total capacity Q and ESR R_0 as well. Plett (2015b) proposed the general framework for this purpose. Nevertheless, it is not implemented in this thesis due to the limitations of the dataset we obtained.

The parameters vary slowly by assumption, and thus the parameter vector θ_k at time instant k is modelled as

$$\theta_k = \theta_{k-1} + r_{k-1} \tag{6.2}$$

where r_{k-1} is a fictitious white noise with zero-mean. The model output equation can be expressed as

$$d_k = g(x_k, u_k, \theta, e_k) \tag{6.3}$$

where $g(\cdot)$ is the output equation of the system model, and e_k represents the sensor noise.

There are two approaches to incorporate state and parameter estimation: joint estimation and dual estimation. Joint estimation combines the state vector x_k and parameter vector θ_k to form augmented dynamics, while in dual estimation, the state dynamics explicitly includes the parameter vector. As they are not implemented in this thesis, for further information, see Appendix B.

In addition to EKF, sigma point Kalman filter (SPKF), also known as unscented Kalman filter (UKF) is another common choice for battery parameter estimation. In summary, for

parameter estimation, the Kalman filter has the advantages of high accuracy and possibility to be used as in-situ estimation. Its drawbacks include high computational effort and requiring a model.

6.2.2 Data-driven methods

The computational complexity of using a nonlinear Kalman filter is relatively high. One alternative is to use simple data-driven methods such as linear regression. Based on the works of Plett (2015b) and Ng et al. (2020), the linear regression is summarized as follows.

Recall Eq. (4.3) and we compute a cell's SOC at time instant $k_2 > k_1$, where the state at k_1 is known.

$$z_{k_2} = z_{k_1} - \frac{1}{Q} \sum_{k=k_1}^{k_2-1} \eta_k i_k \tag{6.4}$$

Rearrange the terms to get

$$-\underbrace{\sum_{k=k_1}^{k_2-1} \eta_k i_k}_{y} = Q \underbrace{(z_{k_2} - z_{k_1})}_{x}, \tag{6.5}$$

The structure becomes a linear equation $y = Qx$. With the values for x and y, we can compute the estimates of Q with regression techniques.

However, in applications, these values are not certain as they both contain errors. The ordinary least square (OLS) approach assumes there is no error on x and models the data as $y = Qx + \Delta y$, where Δy represents the measurement errors. If we want to include the process errors, we can adopt the total least square (TLS) approach which models the data as $y - \Delta y = Q(x - \Delta x)$, where Δx represents the process errors.

In addition to total capacity, linear regression can also be used to predict RUL. Severson et al. (2019) predicts the RUL of Li-ion cells after 100 charge/discharge cycles. The input features include cycle number, voltage, current, and capacity. The prediction error is 9.1%. The simple linear regression model does not require huge computational effort and can be deployed in real-time devices.

Another common data-driven method for SOH estimation and RUL prediction is neural networks, which have already been introduced in Chapter 4, and thus are not discussed in detail in this chapter.

6.3 LSTM-RNN for SOH estimation and RUL prediction

The LSTM-RNN model is used again in this chapter for health diagnosis and failure prediction. The theory, network topology, and hyperparameter training have already been introduced in detail in Section 4.4, and thus are not elaborated on here.
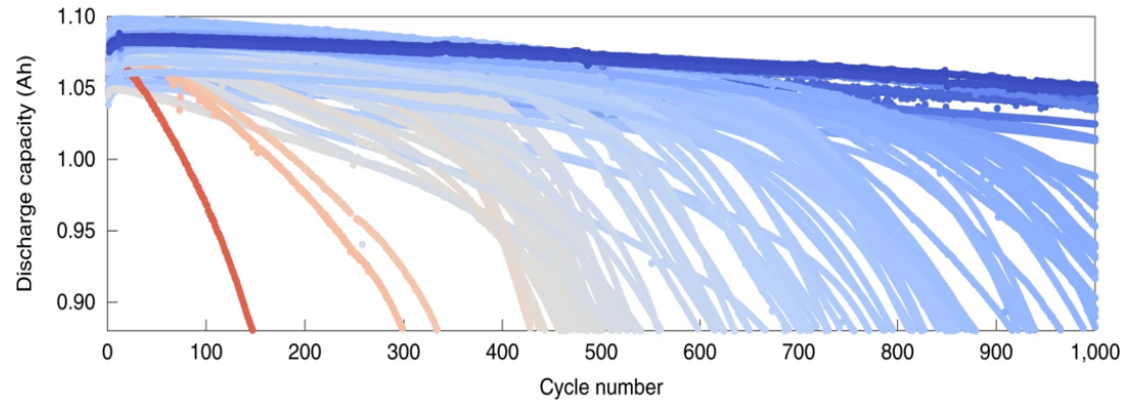
6.3.1 Dataset used

Figure 22: Capacity degradation of all cells (Severson et al. 2019)

The dataset for this chapter is from Severson et al. (2019). 124 LFP/graphite cells (A123 system, model APR18650M1A, 1.1Ah nominal capacity, and 3.3V nominal voltage) were cycled in a battery test chamber until they reached EOL. Fig. 22 shows the capacity degradation for the first 1000 cycles of all cells. Different fast-charging profiles are applied to the cells, while the discharge condition remains identical.

During the test, voltage, current, and capacity are measured and recorded at each time instant. In each cycle, when the cell is charged at 80% SOC, 10 pulses of $\pm 3.6C$ with a width of 30ms are imposed to obtain its internal resistance. Also, the IC/DV analysis is performed in each cycle. The dataset contains up to 96700 cycles. With the massive amount of data, this dataset is suitable for SOH estimation and RUL prediction.

However, this dataset still has its drawbacks. Although all cells are tested in a constant temperature chamber, the temperature measurements for each cell are not "perfectly reliable," as the thermal contact between the thermocouple and the cell can vary substantially, and the thermocouple sometimes loses contact during cycling. Also, the cells are only tested at 30°C. The effect of temperature is not of interest in this dataset. Despite the massive amount of data, it does not contain OCV tests or dynamic tests, which leads to difficulties in system identification. As a result, the EKF for parameter estimation cannot be implemented in this thesis due to the lack of a comprehensive dataset.

6.3.2 Incremental capacity/differential voltage (IC/DV) analysis

The incremental capacity/differential voltage (IC/DV) analysis provides a non-destructive means of characterization of cells and has been widely used for aging mechanism identification and online SOH estimation. The IC is calculated by differentiating the change in battery capacity to the change in terminal voltage for a sufficient small-time interval. At the same time, the DV is defined as the inverse of IC (Li et al. 2019). By differentiating, the voltage plateaus in charge/discharge curves are transformed into identifiable
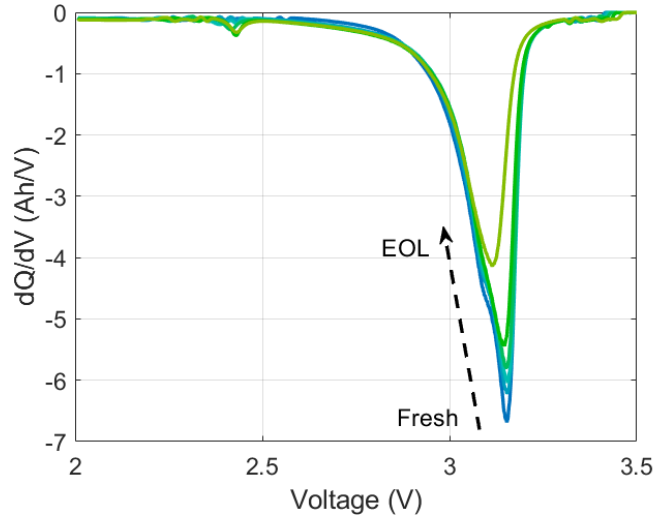
Figure 23: IC curve of one cell from the fresh state to EOL

peaks/valleys in IC/DV curves. The peaks and valleys have their own physical meanings. Valleys in the DV curve indicate phase transitions in the electrodes, while valleys in the IC curve represent the location of a phase equilibrium. The value and location of each peak are essential features containing the aging information of the cell.

Fig. 23 shows the IC curve of one cell in the dataset used. As the cell ages from fresh state to EOL, the valley values (minima) increase, and the corresponding locations on the voltage axis decrease. For different cell chemistries, the curves may have various shapes with multiple peaks/valleys. In that case, all peaks/valleys can become features, although the extracting process will be more difficult.

The IC/DV analysis has several advantages. It is easy to implement in a BMS for on-line SOH estimation by monitoring only two parameters, voltage and charge/discharge capacity. Specifically, IC is more suitable for online SOH estimation. In real-life applications, batteries are not necessarily charged/discharged in full cycles. DV requires a complete cycle, whereas IC can work for partial charging/discharging conditions. Also, IC/DV analysis can all be applied regardless of cell types, sizes, and chemistries.

On the other hand, the drawbacks of IC/DV analysis are significant. For chemistries with large voltage plateaus (e.g. LFP), the dV approximates to zero when using two-point numerical differentiation, yielding results of infinity. Also, it is sensitive to measurement noise, and thus smoothing techniques are required to obtain smooth curves (Li et al. 2019).

6.3.3 Data pre-processing

The data are divided into training set: validation set: test set = 0.8: 0.1: 0.1. A random number generator is used to divide dataset to ensure it is evenly divided. The entire

dataset contains three batches, but the first batch contains several errors, and thus only the second and the third batches are used for testing. The data pre-processing program extracts the minima and the minima location in IC curves, as well as the discharge capacity and the ESR. It then computes the RUL. The cycle number, minima, and the minima location are used as input features, while discharge capacity, ESR, and RUL are to be estimated. Techniques such as standardization are also used to accelerate the convergence speed.

The dataset does not explicitly provide RUL, so we need to compute it. As we know the cycle life of each cell, the RUL is defined as

$$RUL = \text{cycle life} - \text{current cycle number} \tag{6.6}$$

6.3.4 Implementation

The Deep Leaning Toolbox on MATLAB is used to implement the LSTM-RNN. The architecture of the networks is shown in Fig. 24. The amount of data is smaller than in the SOC estimation. Although it enables a higher number of hidden units, it turns out overfitting is a major problem once the number of hidden units exceeds 20. In SOC estimation, the number of hidden units is 120. The difference tells us that the IC curve contains such a massive amount of aging information that it does not require a complex model to explain the relationships. Also, the data used here is less noisy than in the SOC estimation. This explains why the LSTM-RNN here requires less hidden units. The hyperparameters are summarized in Appendix A.
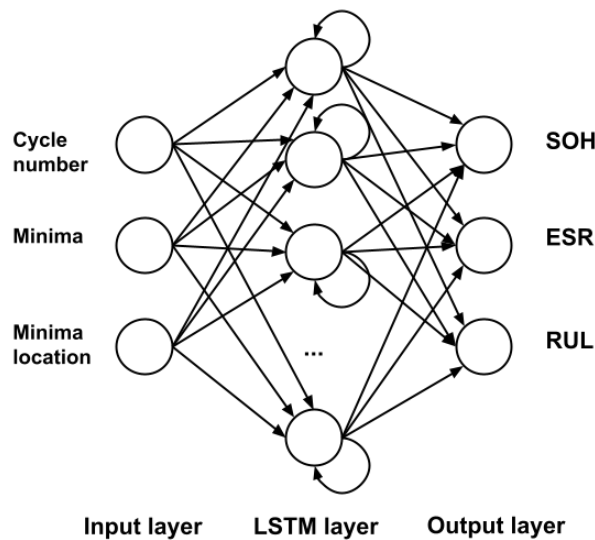

Figure 24: LSTM-RNN topology for estimating/predicting total capacity, ESR and RUL

6.4   Results and discussion

The results for one of the nine cells in the test set are presented in Fig. 25. Table 9 summarizes the performance. Overall, these results indicate that the proposed LSTM-RNN has a good capability in evaluating battery health. However, we can also see that the LSTM-RNN performance in the first 10 cycles is not ideal. For SOH, the error is up to 10% in the first few cycles, while for RUL, the error is near 600. However, in real applications, these estimates are not the only numbers we rely on. Cycle number, which indicates how many cycles the battery has had, is also important when replacing the battery. For instance, a human operator is unlikely to replace a battery with an estimated SOH of 70% if that battery is only on its third cycle. Such a phenomenon can be improved by initialization techniques, which are out of the scope in this thesis. Despite the poor performance in early life, the LSTM-RNN shows a better performance towards the EOL, particularly in RUL prediction. This is helpful for operators to decide when to replace the battery.
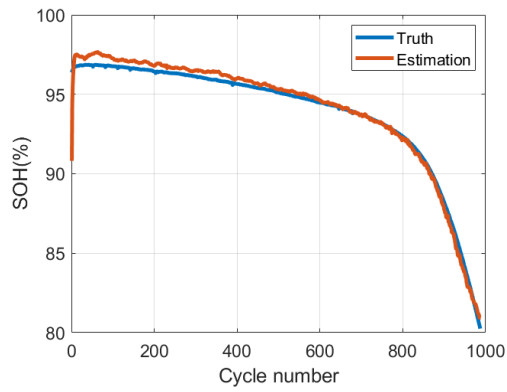
Table 9: LSTM-RNN performance for SOH&ESR estimation and RUL prediction

|	MAE	RMSE	R^2
SOH	0.62%	0.99%	0.99
ESR	0.14mΩ	0.19mΩ	0.98
RUL	64.70	100.99	0.89

The proposed LSTM-RNN for SOH estimation and RUL prediction adopts a different strategy from adaptive filters such as EKF and SPKF: it does not return an estimate at each time step. It is believed the battery health does not decrease rapidly, and evaluating the battery state at each time step would only consume computational resources and provide little information. The proposed LSTM-RNN evaluates the battery health at each cycle, using a few features that the BMS can easily obtain. Besides, the networks contain only a small number of hidden units. The factors mentioned above significantly decrease the computational effort, thus making the method promising for deployment in real applications.

Nevertheless, there are still unanswered questions in this thesis:

- The entire experiment was conducted at 30℃, and there is no available data at different temperatures. Also, due to the loose thermal contacts between the thermocouples and the cells, the temperature measurements are not perfectly reliable. As a result, the effect of temperature remains unclear.
- Alternatively, the LSTM-RNN is able to perform sequence-to-one computation. For each cycle, the voltage and current sequences can be used as input features, returning a total capacity/ESR/RUL estimate. In that case, the networks only use basic measurements to evaluate battery health. Further study can focus on this aspect.

(a) SOH estimation performance
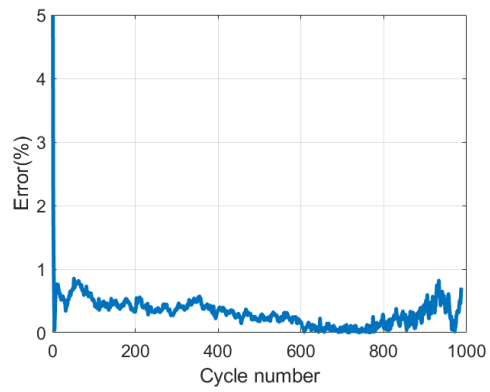
(b) SOH estimation error
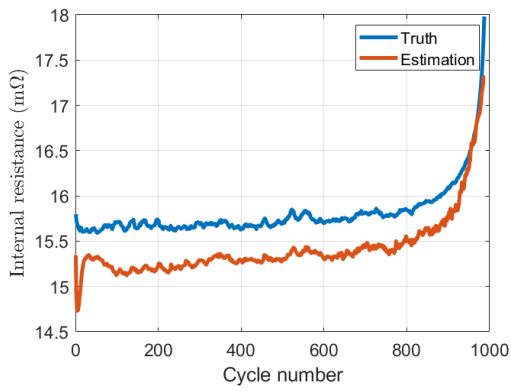
(c) ESR estimation performance
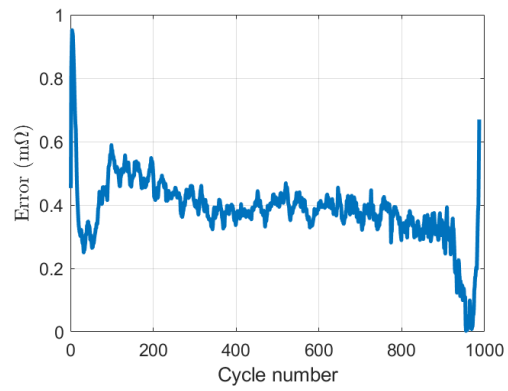
(d) ESR estimation error
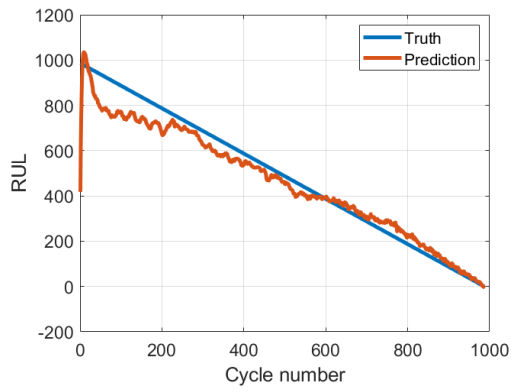
(e) RUL prediction performance
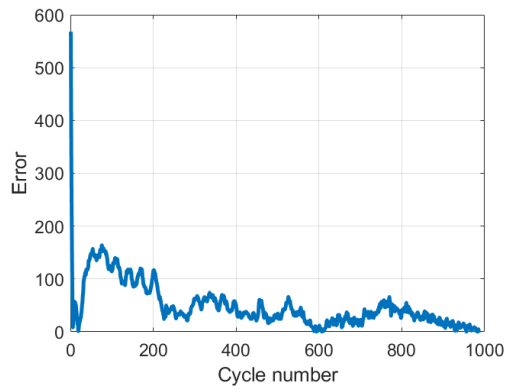
(f) RUL prediction error

Figure 25: LSTM-RNN performance

55

6.5 Summary

In this chapter, the indicators of battery degradation were presented in Section 6.1, and the definition of SOH based on the total capacity was proposed. Section 6.2 introduced two major categories of methods for SOH estimation and RUL prediction: model-based methods and data-driven methods. The LSTM-RNN was again employed to evaluate battery health in Section 6.3. Results show that the LSTM-RNN is a powerful tool for both battery health diagnosis and prognosis with various advantages. Further study can focus on the effect of temperature and on using basic measurements such as voltage and current to evaluate battery health.

Chapter 7

Fault Detection

Safe battery operation can extend the service life of a BESS, and avoid property and human loss. BMS plays an important role in this regard. An important function of the BMS is fault detection, also known as fault diagnosis, which can come from extreme operating conditions, sysyem failure, manufacturing flaws, or battery aging (Wei et al. 2019).

This chapter is organized as follows. Section 7.1 summarizes common faults and analyzes the corresponding causes and consequences. Section 7.2 introduces two categories of fault detection methods: model-based methods and non-model-based methods. A model-based fault detection algorithm - the GLR algorithm - is presented in Section 7.3 and implemented in 7.4.

7.1 Types of fault in a Li-ion BESS

Based on the location of the faults, Li-ion BESS faults can be classified into internal faults and external faults. The mechanisms and failure modes are beyond the scope of the works, and thus they are not discussed in this section. Tran & Fowler (2020) and Helgesen et al. (2019) summarize a number of faults in a Li-ion BESS, and the discussion below is based on their works.

7.1.1 Internal faults

Internal faults occur within the cell. They are difficult to detect as the mechanism within a Li-ion cell is still not fully understood (Tran & Fowler 2020). Typical internal battery faults include overcharge, overdischarge, internal and external short circuit, overheating, and excessive cold.

- **Overcharge.** Overcharge occurs when a battery exceeds its recommended maximum voltage. It is one of the most likely faults that can occur. When a battery is overcharged, internal temperature rises, and the electrolyte is at higher risk of breaking down into its gaseous constituents. It can lead to accelerated degradation and thermal runaway. Also, for a sealed battery, the buildup of gases can cause the

Table 10: Summary of faults in a Li-ion BESS

Faults	Causes	Indicators	Consequences
Overcharge	Sensor faults, inaccuarte SOC estimate, short circuit	SOC, temperature	Thermal runaway, accelerated degradation
Overdischarge	Sensor faults, inaccurate SOC estimate, short circuit	SOC	Accelerated degradation, short circuit
Overheating	Cooling system faults, cell conenction faults, internal/external short circuit	Temperature	Thermal runaway
Excessive cold	Low ambient temperature	Temperature	Efficiency decreasing, formation of dendrites
Internal short circuit	Melting, cell deformation, dendrite formation, compressive shock	Internal resistance	Cell bursting, thermal runaway
External short circuit	Water immersion, collision deformation	Excessive current	Excessive discharge, cell bursting, thermal runaway
Sensor faults	Sensor degradation, connection faults	High residual signal	Overcharge, overdischarge, overheating, cooling system faults
Cooling system faults	Cooling motor or fan failure, temperature sensor faults, broken fuse	High cell temperature	Thermal runaway
Cell connection faults	Vibration and corrosion of the terminals	Increase in cell resistances	Overheating

battery to burst. Common causes for overcharge include the capacity variation of cells in the pack, incorrect voltage or current measurement, inaccurate SOC estimation from the BMS, or a short circuit producing an excessive charge current.

- **Overdischarge.** Similar to overcharge, overdischarge occurs when a battery drops below its recommended minimum voltage. It can also lead to accelerated degradation and decomposition of the electrodes within the battery, which imposes a risk of short circuit. Causes for overdischarge are similar to overcharge, and thus BMS plays an important role in protecting the battery from overcharge and overdischarge.

- **Overheating.** A Li-ion battery can overheat when an alternator's voltage regulator fails, sending a high amount of voltage back to the battery. An internal and external short circuit can produce an excessive current and result in overheating of the battery. Overheating can lead to a significant capacity loss and the breakdown of the internal materials.

- **Excessive cold.** A battery operating below its rated temperature will result in resistance increasing, efficiency decreasing, and formation of dendrites. Lower temperature thresholds vary widely between different cell chemistries and manufacturer recommendations should be followed closely.

- **Internal short circuit.** A short circuit in Li-ion batteries can occur both internally and externally. An internal short circuit occurs when the insulating separator layer between the electrodes fails. This failure of the separator can be attributed to melting due to high temperature, cell deformation, the formation of dendrites, or compressive shock. It could lead to the buildup of off-gas and thermal runaway. Unlike most other faults that show clear symptoms, an internal short circuit is not detectable by the BMS, making it the largest threat to a Li-ion battery system.

- **External short circuit.** An external short circuit often occurs when the tabs are connected directly or by a low resistance path. Water immersion and collision deformation can also lead to an external short circuit. The consequences of an external short circuit include excessive discharge of energy, thermal runaway, and buildup of off-gas. External short circuits can be prevented by passive electrical protections such as fuses and breakers.

7.1.2 External faults

As opposed to internal faults, external faults occur outside the cell, and thus it is easier to detect external faults than internal faults. External faults can have a significant effect on the other functions of the BMS and lead to internal faults. Typical faults include sensor faults, cooling system faults, and cell connection faults.

- **Sensor faults.** Reliable sensors ensure safe battery operation and proper performance. Therefore, it is essential to have a reliable sensor fault diagnostic scheme. A battery cell is generally equipped with a voltage sensor, a current sensor, and a temperature sensor, and each sensor has its independent techniques for fault di-

agnosis. Several scenarios can lead to sensor faults: vibration, collision, electrolyte leakage, loose battery terminals, or corrosion around the battery sensor. A sensor fault can lead to incorrect state estimation and thus hinders the BMS functions.

The temperature sensor is a key component in the battery system as it provides temperature measurements for the BMS and the thermal management system. All faults mentioned in this section will ultimately lead to thermal runaway in the worst case scenario, making the temperature sensor an important component in preventing thermal runaway. A temperature sensor fault can lead to overheating, accelerated degradation, cooling system faults, and even thermal runaway.

Voltage and current measurements from the voltage and current sensors are essential for state estimations, as mentioned in Chapter 4 and 6. Therefore, voltage and current sensor faults can lead to inaccurate state estimates and consequently overcharge, overdischarge, and faulty control actions in the BMS. The method to detect voltage sensor faults is presented and implemented in Section 7.4.

- **Cooling system faults.** The cooling system helps heat dissipation and ensures the battery remains at working temperature. Several scenarios can lead to cooling system faults, such as cooling motor or fan failure, temperature sensor faults, or a broken fuse. A cooling system fault is among the most severe external faults that could occur to a battery system as it directly affects the system's thermal performance and ultimately leads to thermal runaway.

- **Cell connection faults.** As the name suggests, cell connection faults result from a poor electrical connection between the cell terminals. Vibration and corrosion of the terminals will generally lead to this type of fault. Consequently, the cell resistance increases and the BMS gives an uneven balancing current, leading to overheating the cell. Cell connection faults are easy to detect with voltage and temperature sensors.

7.2   Fault detection methods for Li-ion BESS

Fault detection methods for Li-ion BESS can be classified into two categories: model-based and non-model-based. Model-based methods include state estimation, parameter estimation, parity space, and structural analysis (Tran & Fowler 2020), while state estimation is the main focus of this thesis. Implementation of EKF-based voltage sensor fault detection is presented in Section 7.4. Non-model-based methods comprise signal processing and machine learning. The methods apply to both external and internal faults.

Some faults mentioned in the last section, e.g., external short circuit, are easy to detect as the symptom is straightforward. In this example, an excessive current represents the occurrence of an external short circuit. Passive methods, such as fuses and breakers, can respond faster and minimize the potential damage. Therefore, instead of building complex models and developing time-consuming algorithms to detect such faults, it is better to use simple methods. In the following part, only faults that are difficult to detect are considered.
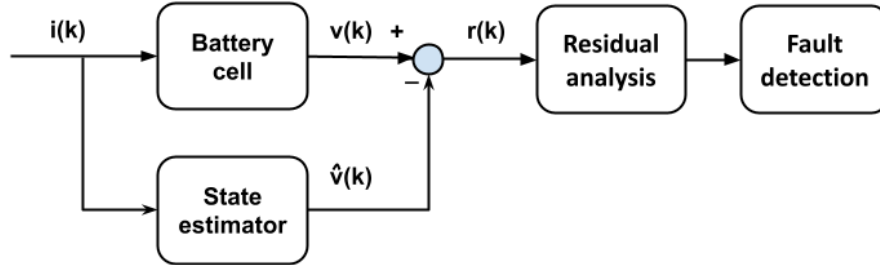
7.2.1 Model-based methods

Figure 26: Schematic for model-based fault detection

Fig. 26 shows the main principle of model-based methods. For a battery cell, the input and output are generally current $i(k)$ and terminal voltage $v(k)$. Provided the same input, the model, which is a state estimator in this case, can also return an output voltage $\hat{v}(k)$. The residual $r(k) = v(k) - \hat{v}(k)$ is used to detect fault. If we assume the current sensor functions properly and the model is correct, when $r(k)$ is beyond the predefined range, it indicates a voltage sensor fault. In Section 7.4, we will further discuss how to determine this range with generalized likelihood ratio test (GLRT). Besides, as a state estimator can estimate the SOC, an accurate SOC estimation can also prevent overcharge and overdischarge.

Other battery models can be applied to detect various faults. Alavi et al. (2013) proposed a particle-filtering-based estimation technique to detect plating of metallic lithium for Li-ion batteries. They used an electrochemical model to the algorithm, and this method is effective in detecting Li plating. However, an electrochemical model is computationally intensive, making it unrealistic for real-time applications.

Model-based methods can quickly detect and isolate a fault in real-time but require high modeling accuracy (Tran & Fowler 2020). Further research should focus on battery failure modes to develop a precise yet efficient battery model.

7.2.2 Non-model-based methods

Non-model-based methods include signal processing and machine learning. These methods can avoid the difficult requirements for battery modeling and improve the fault detection accuracy. But they generally require a huge amount of fault data, and very often it is not available. Particularly in the marine sector, the data are usually confidential. As of now, there is no available public dataset in the marine sector for fault detection. Also, these methods are often computationally intensive, and therefore, they are impractical for real-time applications in BMS. In recent years, different machine learning methods are implemented for fault detection, such as fuzzy logic (Muddappa & Anwar 2014), random forest (Yang et al. 2018), and neural networks (Zhao et al. 2017).

7.3 Fault detection algorithm

Recall the voltage residual $r(k) = v(k) - \hat{v}(k)$ (Fig. 26). By intuition, a voltage sensor fault occurs when $r(k)$ exceeds a certain threshold; this is a straightforward but not practical method, as the voltage sensor is affected by noise and its output fluctuates over time. Thus it is difficult to determine the threshold. Blanke et al. (2006) proposed a statistics-based framework which uses a decision function for fault detection and the following discussion is based on their works.

Two types of algorithms aim to solve the fault detection problem: cumulative sum (CUSUM) and generalized likelihood ratio (GLR). Both algorithms rely on Neyman-Pearson's method. The CUSUM can detect known changes, while GLR focuses on unknown changes. Each algorithm can be further classified into scalar and vector cases depending on the number of fault indicators. The change is usually unknown for a voltage sensor fault, and the voltage residual is the only indicator. With regards to this, the scalar GLR algorithm is introduced and implemented in this thesis. A formal problem statement is first presented in this section.

7.3.1 Problem statement

Before introducing the GLR algorithm, we need to give a formal problem statement. Given a sequence of independent random variables $r(1), ..., r(k)$ with probability density function $p_\theta(x)$ depending on one scalar parameter θ. Choose at time instant k between the following two hypotheses:

$\mathcal{H}_0$(the nominal case) : $\theta = \theta_0$ for $1 \leq i \leq k$

$\mathcal{H}_1$(the faulty case) : $\theta = \theta_0$ for $1 \leq i \leq k_0 - 1$ and $\theta = \theta_1$ for $k_0 \leq i \leq k$, where

the time instant k_0 is unknown.

Without a detailed definition, a decision function and the threshold are denoted as $g(k)$ and h. At each time instant, make the following decisions:

$$\text{if } g(k) \leq h \text{ accept } \mathcal{H}_0$$

$$\text{if } g(k) > h \text{ accept } \mathcal{H}_1 .$$

When $\mathcal{H}_1$ is accepted, $k_a = k$ is the instant when fault occurs. The objective of the algorithm is to find a sequence of k_a. Next on, we will introduce how to define $g(k)$ as well as how h is determined.

7.3.2 The generalized likelihood ratio (GLR) algorithm

Let j be a hypothetical change time, the log-likelihood ratio between $\mathcal{H}_0$ and $\mathcal{H}_1$ with $k_0 = j$ is given as

$$\Lambda_1^k(j) = \frac{\displaystyle\prod_{i=1}^{j-1} p_{\theta_0}(r(i)) \prod_{i=j}^{k} p_{\theta_1}(r(i))}{\displaystyle\prod_{i=1}^{k} p_{\theta_0}(r(i))} \tag{7.1}$$

The cumulative sum of log-likelihood ratios is written as:

$$S_j^k(\theta_1) = \ln\Lambda_1^k(j) = \sum_{i=j}^{k} \ln\frac{p_{\theta_1}(r(i))}{p_{\theta_0}(r(i))} \tag{7.2}$$

The optimal decision function for this problem is

$$g(k) = \max_{1 \le j \le k} \max_{\theta_1} S_j^k(\theta_1) \tag{7.3}$$

The maximization in Eq. (7.3) is performed over all possible time instants, and this will significantly increase the computational effort as time elapses. Therefore, we restrict the computation to the last M time instants. The hypotheses are rewritten as:

$$\mathcal{H}_0 : \theta = \theta_0 \text{ for } k - M + 1 \le i \le k,$$

$$\mathcal{H}_1 : \theta = \theta_1 \text{ for } k - M + 1 \le i \le k.$$

The corresponding decision function is denoted as $g_M(k)$:

$$g_M(k) = \max_{k-M+1 \le j \le k} \max_{\theta_1} S_j^k(\theta_1) \tag{7.4}$$

where M is termed *window length*.

For a change in the mean of a Gaussian sequence, $g_M(k)$ takes the following form:

$$g_M(k) = \frac{1}{2\sigma^2 M} \left[\sum_{i=k-M+1}^{k} (r(i) - \mu_0) \right]^2 \tag{7.5}$$

where σ and μ_0 denote the variance and the mean of the sequence, respectively. The

proof is provided in Appendix C.1.

So far, we have derived the expression for the decision function, but the threshold h and the window length M remain unknown. Limited by space, the procedure to design these two parameters can be found in Appendix C.2. The GLR algorithm is summarized as follows:

GLR algorithm

Given:

1. A sequence of data $r(1), ..., r(k)$ with probability density function $p_\theta(r)$ depending on the scalar parameter θ.
2. A threshold h and a window length M.

At each time instant k:

Compute $g_M(k)$ with Eq. (7.5). If $g_M(k) > h$, generate an alarm and provide the time instant $k_a = k$.

Return:

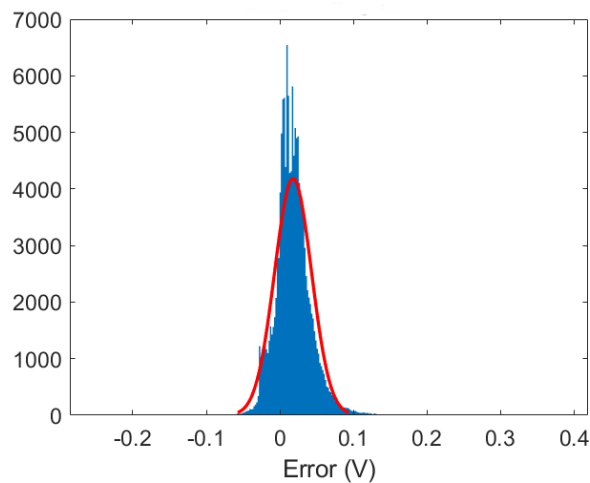A sequence of alarm time instants k_a.

Figure 27: Residual distribution

7.4 EKF-based voltage sensor fault detection

Based on the EKF developed in Chapter 4, we implement the GLR algorithm to detect voltage sensor faults. First, we need to confirm the residual $r(k) = v(k) - \hat{v}(k)$ follows a Gaussian distribution. The drive cycle used in this section is also LA92. The voltage measurement, estimates using EKF, and the residual are presented in Fig. 28(a) and (b).

Fig. 27 shows that we can approximate the residual distribution as a Gaussian distribution, with mean $\mu_0 = 0.0198$ and standard deviation $\sigma = 0.1369$. We use subscript 0 for nominal case, and 1 for faulty case.

As there are no faults in the original data, we need to create some by manipulating the data. Let the voltage sensor fault occur between 25.0 and 25.3 $\min$, and we multiply the voltage measurement data by 1.1 to create faults. The voltage data after manipulation are shown in Fig. 28(c) and (d). The mean of faulty voltage $\mu_1 = -0.403$.

(a) Voltage measurement vs estimation using EKF

(b) Voltage residuals

(c) Voltage measurement vs estimation using EKF after manipulation

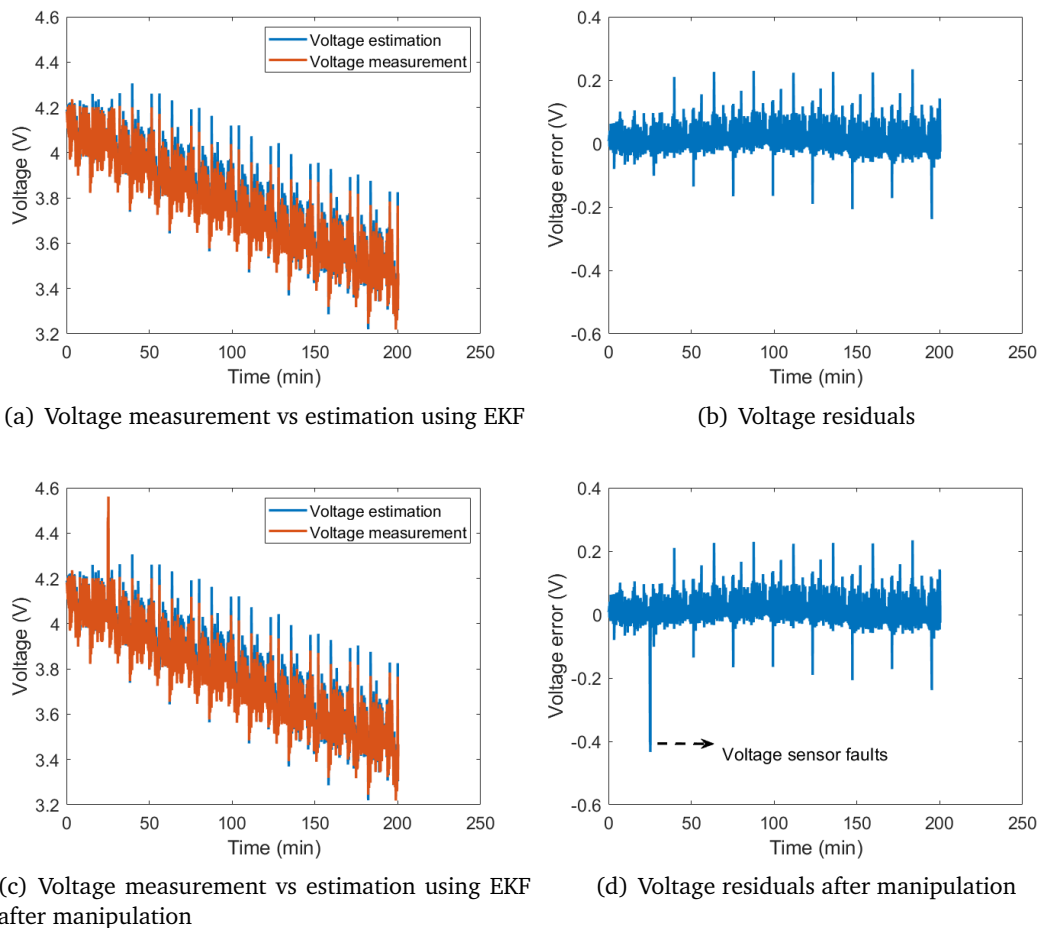(d) Voltage residuals after manipulation

Figure 28: Manipulation of data to mimic voltage sensor faults

After we compute the statistics of the data, with the GLR design process, we obtain both the threshold $h = 9.2$ and the window length $M = 5$. With these statistics and parameters, we can start testing the algorithm.
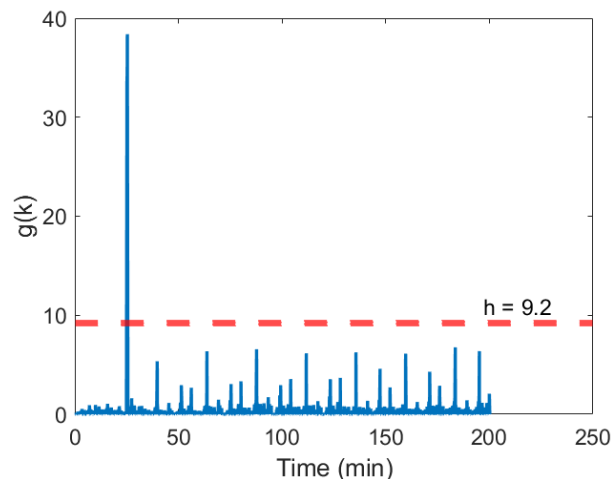

Figure 29: GLR algorithm test results

In the main loop of EKF, $g(k)$ is computed at each time instant $k > 5$ using Eq. (7.5). Once $g_M(k) > h$, the program sends an alarm along with the current time instant k_a. An array *alarm* is used to store the alarm signal. The $g_M(k)$ value over all time instants is shown in Fig. 29. The faulty voltage begins at time instant $k = 15000$ and ends at $k = 15200$, while the alarm signal begins at $k = 15003$ and ends at $k = 15203$. The results show that the GLR algorithm provides a systematic approach for fault detection. Although the window technique can decrease computational effort, it also introduces time delay when detecting the fault and when the fault is clear, which in this case is $0.3s$. Blanke et al. (2006) also provides the approach to estimate the fault occurrence time. However, the fault occurrence time is likely unnecessary, and requires a significant computational effort. In this thesis, the precise fault occurrence time is not considered, and the short time delay is within the acceptable range. Therefore, the fault occurrence time estimation is not implemented.

7.5 Summary

For a Li-ion BESS, faults can be categorized into internal faults and external faults. Section 7.1 summarized common faults and analyzed the corresponding causes and consequences. Section 7.2 introduced two categories of fault detection methods: model-based methods and non-model-based methods. A model-based fault detection algorithm - the GLR algorithm - was presented in Section 7.3 and implemented in 7.4.

In simple residual analysis methods, when the residual $r(k)$ exceeds a specific value, the system returns an alarm. However, these methods fail to consider measurement

noise, and the threshold is designed empirically. The GLR algorithm provides a systematic approach to detect faults in a stochastic system, and the parameters are designed based on statistics. The test results proved the algorithm's capability in detecting voltage sensor fault, and it seems promising to apply it in actual Li-ion BESS.

Chapter 8

Conclusion and Future Work

8.1 Conclusion

The short-term drive cycle performance dataset contains experimental data, including drive cycle tests, OCV tests, dynamic tests, and HPPC tests. The OCV test and dynamic test are used for battery model parameter identification, while the drive cycle tests are used for SOC estimation with two methods. The model-based method - EKF - achieves a low MAE of 0.64% on nine drive cycles, while the machine learning method - LSTM-RNN - has an MAE of 0.84% on the test set. Both methods show good performance in SOC estimation, but they both have strengths and weaknesses. The states and output estimation of the EKF can be further applied in power limit estimation and fault detection. Also, over the years, it has been widely applied and approved in practice. However, its model parameters need to be identified under the system identification framework, which requires additional laboratory tests and workload. In contrast, the LSTM-RNN can map raw measurement data directly to SOC without a battery model. Also, it is the battery system's nature that it can collect a massive amount of data in a short duration, and thus machine learning methods have the potential to be used in practice. However, unlike the EKF can also be applied to power limit estimation and fault detection, the LSTM-RNN proposed here is limited to SOC estimation. For specific purposes, customized LSTM-RNN should be established.

The HPPC test in the dataset is used for power limit estimation. This thesis showcases how power limit can be determined using the HPPC test data with a simplified ECM and drive cycle test data with a complete ECM. An accurate power limit estimation ensures a safe and optimal operation of the batteries.

Another dataset used in this thesis is the long-term degradation dataset. 124 cells are cycled until the EOL in this dataset, and thus it is ideal for battery health diagnosis (SOH estimation) and failure prediction (RUL prediction). The proposed LSTM-RNN uses a small number of input features from IC analysis and delivers high accuracy. For SOH estimation, the networks achieve an MAE of 0.62%, and for RUL prediction, the MAE is 64.7 cycles. The small number of input features, the accessibility to these features during

each cycle, and the simple network structure make LSTM-RNN a promising method in practice.

Fault detection is another focus of this thesis. Various faults that can occur in a Li-ion BESS are investigated and presented. Combined with the EKF proposed earlier, the GLR algorithm is introduced and implemented to detect voltage sensor faults. As there are no faults in the original dataset, the voltage data are manipulated to simulate a voltage sensor fault. The algorithm provides a systematic approach for residual analysis. By restricting the computation to a specific window length, the computational effort significantly decreases, and the algorithm is able to detect voltage sensor fault with a short time delay of 0.3s.

8.2   Future work

Although the obtained results are equally applicable, it is still preferred to use available data from the marine industry. Also, due to the particularities of the datasets, a different dataset is used for SOH estimation and RUL prediction. This makes it impossible to consider the cell aging effect when estimating SOC. Also, it reduces the consistency of the thesis to a certain extent. If possible, future research work needs to be conducted in one dataset from the marine industry.

In addition, the effect of temperature is not taken into account for both SOC and SOH estimation in this thesis due to the lack of time. Future experiments using a broader range of temperature could shed more light on the effect of temperature.

Moreover, due to the lack of fault data, the faults are manipulated manually to test the algorithm. Future research should apply data obtained from practice for fault detection if possible.

Bibliography

ABB Containerized maritime energy storage (n.d.).
   URL: *https://new.abb.com/marine/systems-and-solutions/electric-solutions*

Alavi, S. M., Samadi, M. F. & Saif, M. (2013), Plating mechanism detection in lithium-ion batteries, by using a particle-filtering based estimation technique, *in* '2013 American Control Conference', IEEE, pp. 4356–4361.

Antón, J. Á., Nieto, P. G., de Cos Juez, F., Lasheras, F. S., Vega, M. G. & Gutiérrez, M. R. (2013), 'Battery state-of-charge estimator using the svm technique', *Applied Mathematical Modelling* **37**(9), 6244–6253.

Batteries on board ocean-going vessels (n.d.).
   URL: *https://www.man-es.com/docs/default-source/marine/tools/batteries-on-board-ocean-going-vessels.pdf?sfvrsn=deaa76b8_14*

BatteryBits (2020), 'Comparison of open datasets for lithium-ion battery testing'.
   URL: *https://medium.com/batterybits/comparison-of-open-datasets-for-lithium-ion-battery-testing-fd0de091ca2*

Bermejo, D., Fraile-Ardanuy, J., Castaño-Solis, S., Merino, J. & Álvaro-Hermana, R. (2018), 'Using dynamic neural networks for battery state of charge estimation in electric vehicles', *Procedia computer science* **130**, 533–540.

Blanke, M., Kinnaert, M., Lunze, J., Staroswiecki, M. & Schröder, J. (2006), *Diagnosis and fault-tolerant control*, Vol. 2, Springer.

Chemali, E., Kollmeyer, P. J., Preindl, M., Ahmed, R. & Emadi, A. (2017), 'Long short-term memory networks for accurate state-of-charge estimation of li-ion batteries', *IEEE Transactions on Industrial Electronics* **65**(8), 6730–6739.

Chemali, E., Kollmeyer, P. J., Preindl, M. & Emadi, A. (2018), 'State-of-charge estimation of li-ion batteries using deep neural networks: A machine learning approach', *Journal of Power Sources* **400**, 242–255.

Corvus Energy introduces standardized ISO footprint containerized battery room solutions (2021).
   URL: *https://corvusenergy.com/corvus-energy-introduces-standardized-iso-footprint-containerized-battery-room-solutions/*

Eaton Containerized energy storage system (n.d.).
   URL: *https://www.eaton.com/content/dam/eaton/products/energy-storage/xstorage-container/eaton-xStorage-container-flyer-SA701002EN-en-gb.pdf*

Frankforter, K. J., Tejedor-Tejedor, M. I., Anderson, M. A. & Jahns, T. M. (2020), 'Investigation of hybrid battery/ultracapacitor electrode customization for energy storage applications with different energy and power requirements using hppc cycling', *IEEE Transactions on Industry Applications* **56**(2), 1714–1728.

Gear, L. (2020), 'Electric ships: Battery behemoths'.
   URL: *https://www.electricvehiclesresearch.com/articles/21489/electric-ships-battery-behemoths/*

Helgesen, H., Haugom, G., Sverud, T., Henningsgård, S., Gully, B., Mjøs, N., Langli, A. & Frithiof, N. (2019), Study on electrical energy storage for ships, Technical report, DNV GL AS Maritime.

Hochreiter, S. & Schmidhuber, J. (1997), 'Long short-term memory', *Neural computation* **9**(8), 1735–1780.

Hu, C. & Jain (2015), 'Online estimation of lithium-ion battery capacity using sparse bayesian learning', *Journal of Power Sources* **289**, 105–113.

Hu, J., Hu, J., Lin, H., Li, X., Jiang, C., Qiu, X. & Li, W. (2014), 'State-of-charge estimation for battery management system using optimized support vector machine for regression', *Journal of Power Sources* **269**, 682–693.

Hu, X., Li, S. E. & Yang, Y. (2015), 'Advanced machine learning approach for lithium-ion battery state estimation in electric vehicles', *IEEE Transactions on Transportation electrification* **2**(2), 140–149.

Kang, L., Zhao, X. & Ma, J. (2014), 'A new neural network model for the state-of-charge estimation in the battery degradation process', *Applied Energy* **121**, 20–27.

Kyunghwa Kim, Kido Park, Jongwoo Ahn, Gilltae Roh & Kangwoo Chun (2016), A study on applicability of battery energy storage system (bess) for electric propulsion ships, *in* '2016 IEEE Transportation Electrification Conference and Expo, Asia-Pacific (ITEC Asia-Pacific)', pp. 203–207.

Li, Y., Liu, K., Foley, A. M., Zülke, A., Berecibar, M., Nanini-Maury, E., Van Mierlo, J. & Hoster, H. E. (2019), 'Data-driven health estimation and lifetime prediction of lithium-ion batteries: A review', *Renewable and sustainable energy reviews* **113**, 109254.

Lu, L., Han, X., Li, J., Hua, J. & Ouyang, M. (2013), 'A review on the key issues for lithium-ion battery management in electric vehicles', *Journal of power sources* **226**, 272–288.

MF Ampere (n.d.).
  URL: *https://en.wikipedia.org/wiki/MVAmpere*

MIT, E. T. (2008), 'A guide to understanding battery specifications'.
  URL: *http://web.mit.edu/evt/summary$_b$attery$_s$pecif ications.pdf*

Muddappa, V. K. & Anwar, S. (2014), Electrochemical model based fault diagnosis of li-ion battery using fuzzy logic, *in* 'ASME 2014 International Mechanical Engineering Congress and Exposition', American Society of Mechanical Engineers Digital Collection.

Mutarraf, M. U., Terriche, Y., Niazi, K. A. K., Vasquez, J. C. & Guerrero, J. M. (2018), 'Energy storage systems for shipboard microgrids—a review', *Energies* **11**(12), 3492.

Ng, M.-F., Zhao, J., Yan, Q., Conduit, G. J. & Seh, Z. W. (2020), 'Predicting the state of charge and health of batteries using data-driven machine learning', *Nature Machine Intelligence* pp. 1–10.

Oberhaus, D. (2020), 'Want electric ships? build a better battery'.
  URL: *https://www.wired.com/story/want-electric-ships-build-a-better-battery/*

Olah, C. (2015), 'Understanding lstm networks'.
  URL: *https://colah.github.io/posts/2015-08-Understanding-LSTMs/*

Plett, G. L. (2015*a*), *Battery management systems, Volume I: Battery modeling*, Artech House.

Plett, G. L. (2015*b*), *Battery management systems, Volume II: Equivalent-circuit methods*, Artech House.

Rules for classification - ships (2019*a*), Technical report, DNV GL AS.

Rules for classification - ships (2019*b*), Technical report, DNV GL AS.

Sahinoglu, G. O., Pajovic, M., Sahinoglu, Z., Wang, Y., Orlik, P. V. & Wada, T. (2017), 'Battery state-of-charge estimation based on regular/recurrent gaussian process regression', *IEEE Transactions on Industrial Electronics* **65**(5), 4311–4321.

Severson, K. A., Attia, P. M., Jin, N., Perkins, N., Jiang, B., Yang, Z., Chen, M. H., Aykol, M., Herring, P. K., Fraggedakis, D. et al. (2019), 'Data-driven prediction of battery cycle life before capacity degradation', *Nature Energy* **4**(5), 383–391.

Tong, S., Lacap, J. H. & Park, J. W. (2016), 'Battery state of charge estimation using a load-classifying neural network', *Journal of Energy Storage* **7**, 236–243.

Tran, M.-K. & Fowler, M. (2020), 'A review of lithium-ion battery fault diagnostic algorithms: Current progress and future challenges', *Algorithms* **13**(3), 62.

Types of Lithium-ion (n.d.).
 URL: *https://batteryuniversity.com/learn/article/types$_o f_l$ithium$_i$on*

Uninterruptible power supply (n.d.).
 URL: *https://en.wikipedia.org/wiki/Uninterruptible$_p$ower$_s$upply*

Wei, J., Dong, G. & Chen, Z. (2019), 'Model-based fault diagnosis of lithium-ion battery using strong tracking extended kalman filter', *Energy Procedia* **158**, 2500–2505.

World's largest electric ferry launches in Norway (2021).
 URL: *https://www.electrive.com/2021/03/02/worlds-largest-electric-ferry-yet-goes-into-service-in-norway/*

Wu, T., Wang, M., Xiao, Q., Wang, X. et al. (2012), 'The soc estimation of power li-ion battery based on anfis model', *Smart Grid and Renewable Energy* **3**(1), 51–55.

Yang, R., Xiong, R., He, H. & Chen, Z. (2018), 'A fractional-order model-based battery external short circuit fault diagnosis approach for all-climate electric vehicles application', *Journal of cleaner production* **187**, 950–959.

Zhao, Y., Liu, P., Wang, Z., Zhang, L. & Hong, J. (2017), 'Fault and defect diagnosis of battery for electric vehicles based on big data analysis methods', *Applied Energy* **207**, 354–362.

Appendix A

Hyperparameters for neural network training

Table 11: LSTM-RNN hyperparameters for SOC estimation

Hyperparameters	Value
Number of hidden units	120
Maximum epochs	100
Minimum batch size	256
L2 regularization factor	0.001
Initial learning rate	0.005
Learning rate drop period	50
Learning rate drop factor	0.1

Table 12: LSTM-RNN hyperparameters for SOH estimation and RUL prediction

Hyperparameters	Value
Number of hidden units	15
Maximum epochs	300
Minimum batch size	64
L2 regularization factor	0.001
Initial learning rate	0.01
Learning rate drop period	150
Learning rate drop factor	0.1

Appendix B

Joint extended Kalman filter (JEKF) for state and parameter estimation

This method is adapted from Plett (2015*b*), Chapter 4.

The state-space model is written as:

$$
\begin{bmatrix} x_k \\ \theta_k \end{bmatrix} = \begin{bmatrix} f\left(x_{k-1}, u_{k-1}, w_{k-1}, \theta_{k-1}\right) \\ \theta_{k-1} + r_{k-1} \end{bmatrix} \tag{B.1}
$$

$$
y_k = h\left(x_k, u_k, v_k, \theta_k\right) \tag{B.2}
$$

where states, parameters, and output are denoted as x_k, θ_k, y_k, respectively. w_k, r_k and v_k are independent, Gaussian noise processes with means $\bar{w}$, zero, and $\bar{v}$, and covariance matrices $\Sigma_{\tilde{w}}, \Sigma_{\tilde{r}}$, and $\Sigma_{\tilde{v}}$, respectively. Let $\mathbf{X}_k = \left[x_k^T, \; \boldsymbol{\theta}_k^T\right]^T$, $\mathbf{W}_k = \left[w_k^T, \; r_k^T\right]^T$ and $\Sigma_{\widetilde{\mathbf{W}}} = \mathrm{diag}\left(\Sigma_{\tilde{w}}, \Sigma_{\tilde{r}}\right)$, we have

$$
\mathbf{X}_k = \mathbf{F}\left(\mathbf{X}_{k-1}, u_{k-1}, \mathbf{W}_{k-1}\right) \tag{B.3}
$$

$$
y_k = h\left(\mathbf{X}_k, u_k, v_k\right) \tag{B.4}
$$

Define the following variables:

$$
\begin{aligned}
\hat{A}_k &= \left.\frac{dF(X_k, u_k, \, W_k)}{dX_k}\right|_{X_k = \hat{\mathbf{X}}_k^+} & \hat{B}_k &= \left.\frac{dF(X_k, u_k, w_k)}{dW_k}\right|_{W_k = \overline{\mathbf{W}}_k} \\
\hat{C}_k &= \left.\frac{dh(X_k, u_k, v_k)}{dX_k}\right|_{X_k = \hat{X}_k^-} & \hat{D}_k &= \left.\frac{dh(X_k, u_k, v_k)}{dv_k}\right|_{v_k = \bar{v}_k}
\end{aligned} \tag{B.5}
$$

Initialization: for $k = 0$, set

$$\hat{\mathbf{X}}_0^+ = \mathbb{E}\left[\mathbf{X}_0\right] \tag{B.6}$$

$$\Sigma_{\tilde{X},0}^+ = \mathbb{E}\left[\left(\mathbf{X}_0 - \hat{\mathbf{X}}_0^+\right)\left(\mathbf{X}_0 - \hat{\mathbf{X}}_0^+\right)^T\right] \tag{B.7}$$

Main loop: for $k = 1, 2, ...$, compute:

State estimate time update: $\hat{\mathbf{X}}_k^- = F\left(\hat{\mathbf{X}}_{k-1}^+, u_{k-1}, \mathbf{W}_{k-1}\right)$ (B.8)

Error covariance time update: $\Sigma_{\tilde{\mathbf{X}},k}^- = A_{k-1}\Sigma_{\tilde{\mathbf{X}},k-1}^+ A_{k-1}^T + \hat{B}_{k-1}\Sigma_{\widetilde{W}}\hat{B}_{k-1}^T$ (B.9)

Output estimate: $\hat{y}_k = h\left(\hat{\mathbf{X}}_k^-, u_k, \bar{v}_k\right)$ (B.10)

Estimator gain matrix: $L_k = \Sigma_{\tilde{\mathbf{X}},k}\hat{C}_k^T\left[\hat{C}_k\Sigma_{\tilde{\mathbf{X}},k}\hat{C}_k^T + \hat{D}_k\Sigma_{\tilde{v}}\hat{D}_k^T\right]^{-1}$ (B.11)

State estimate meas. update: $\hat{\mathbf{X}}_k^+ = \hat{x}_k^- + L_k\left(y_k - \hat{y}_k\right)$ (B.12)

Error covariance meas. update: $\Sigma_{\tilde{X},k^+} = \Sigma_{\tilde{X}_k^- - L_k}\Sigma_{\tilde{y},k L_k^T}$ (B.13)

Appendix C

The GLR algorithm

C.1 Proof of $g_M(k)$ for the change of mean in a Gaussian sequence

Given: a Gaussian sequence $r(k)$ with independent and identically distributed increments.

Prove: the decision function $g_M(k)$ takes the form:

$$g_M(k) = \frac{1}{2\sigma^2 M}\left[\sum_{i=k-M+1}^{k}(r(i) - \mu_0)\right]^2$$

Proof:

For a Gaussian sequence, the cumulative sum of log-likelihood ratios is written as:

$$S_k(\mu_1) = \sum_{i=j}^{k}\ln\frac{p_{\theta_1}(r(i))}{p_{\theta_0}(r(i))} = \frac{\mu_1 - \mu_0}{\sigma^2}\sum_{i=k-M+1}^{k}\left(r(i) - \frac{\mu_1 + \mu_0}{2}\right) \tag{C.1}$$

To maximize $S_k(\mu_1)$ with respect to μ_1, we need to find $\frac{\partial S_k(\mu_1)}{\partial \mu_1} = 0$.

$$\frac{\partial S_k(\mu_1)}{\partial \mu_1} = \frac{1}{\sigma^2} \sum_{i=k-M+1}^{k} \left(r(i) - \frac{\mu_1 + \mu_0}{2} \right) - \frac{\mu_1 - \mu_0}{\sigma^2} \frac{M}{2} = 0$$

$$\Rightarrow \sum_{i=k-M+1}^{k} r(i) - \sum_{i=k-M+1}^{k} \frac{\hat{\mu}_1 + \mu_0}{2} - (\hat{\mu}_1 - \mu_0) \frac{M}{2} = 0$$

$$\Rightarrow \sum_{i=k-M+1}^{k} r(i) - (\hat{\mu}_1 + \mu_0) \frac{M}{2} - (\hat{\mu}_1 - \mu_0) \frac{M}{2} = 0$$

$$\Rightarrow \hat{\mu}_1 = \frac{1}{M} \sum_{i=k-M+1}^{k} r(i)$$

Substitute $\hat{\mu}_1$ into C.1, and yield

$$S_k(\hat{\mu}_1) = \frac{1}{\sigma^2} \left(\frac{1}{M} \sum_{i=k-M+1}^{k} r(i) - \mu_0 \right) \sum_{i=k-M+1}^{k} \left(r(i) - \frac{1}{2} \left(\frac{1}{M} \sum_{i=k-M+1}^{k} r(i) + \mu_0 \right) \right)$$

Note that

$$\sum_{i=k-M+1}^{k} \frac{1}{M} \sum_{i=k-M+1}^{k} r(i) = \sum_{i=k-M}^{k} r(i),$$

$$\frac{1}{M} \sum_{i=k-M+1}^{k} \mu_0 = \mu_0$$

Thus we have

$$\max_{\mu_1} S_k(\mu_1) = S_k(\hat{\mu}_1) = \frac{1}{2\sigma^2 M} \left(\sum_{k-M+1}^{k} (r(i) - \mu_0)^2 \right) \tag{C.2}$$

$$g_M(k) = \max_{\mu_1} S_k(\mu_1) = g_M(k) = \frac{1}{2\sigma^2 M} \left[\sum_{i=k-M+1}^{k} (r(i) - \mu_0) \right]^2 \tag{C.3}$$

C.2 GLR design methodology

The objective is to design the threshold h and window length M to meet a given probability P_F of false alarm, and a probability P_D of detection of a change in mean from μ_0 to μ_1.

Denote the log-likelihood taken over a window length M by S_M,

$$
\begin{aligned}
S_M(k) &= \sum_{i=k-M+1}^{k} \ln \frac{p_{\theta_1}(r(i))}{p_{\theta_0}(r(i))} \\
&= \frac{1}{\sqrt{M}\sigma} \left[\sum_{i=k-M+1}^{k} (r(i) - \mu_0) \right]
\end{aligned}
$$

Note that $S_M(k) = 2\sqrt{g(k)}$, and it has the following probability:

$$
p(S_M(k)) = \mathcal{N}(0,1) \text{ under } \mathcal{H}_0
$$

$$
p(S_M(k)) = \mathcal{N}\left(\frac{\sqrt{M}(\mu_1 - \mu_0)}{\sigma}, 1 \right) \text{ under } \mathcal{H}_1
$$

The probability law for $g_M(k)$ is given by

$$
p(2g_M(k)) = \chi_1^2 \text{ under } \mathcal{H}_0 \tag{C.4}
$$

$$
p(2g_M(k)) = \chi_1^2 \left(\frac{M(\mu_1 - \mu_0)^2}{\sigma^2} \right) \text{ under } \mathcal{H}_1 \tag{C.5}
$$

where $\chi_1^2(x)$ denotes the chi-square distribution with one degree of freedom with the non-centrality parameter x.

To enforce the given probabilities of false and correct detection, they are given as:

$$
P_F = P(g > h \mid \mathcal{H}_0) = \int_h^\infty p(g \mid \mathcal{H}_0)\, dg \tag{C.6}
$$

$$
P_D = P(g \geq h \mid \mathcal{H}_1) = \int_h^\infty p(g \mid \mathcal{H}_1)\, dg \tag{C.7}
$$

where $p(2g \mid \mathcal{H}_0)$ and $p(2g \mid \mathcal{H}_1)$ denote the probability density function of the test function, 2g, conditioned on $\mathcal{H}_0$ and $\mathcal{H}_1$, respectively. Accounting to the previously deter-

mined probability density functions C.4 and C.5, yield:

$$\int_{2h}^{\infty} p_{\chi_1^2}(X)dX = \alpha \tag{C.8}$$

$$\int_{2h}^{\infty} p_{\chi_1^2}\left(X; \frac{M(\mu_1 - \mu_0)^2}{\sigma^2}\right) dX = \beta \tag{C.9}$$

If data are available for both $\mathcal{H}_0$ and $\mathcal{H}_1$ cases, the cumulative density functions $F(g_M \mid \mathcal{H}_0; M)$ and $F(g_M \mid \mathcal{H}_1; M)$ can be estimated from these data for different values of the window length M. From these cumulative density functions, the threshold h and window length M can be determined to achieve a required probability of false alarm α and a required probability of correct detection β. They can be expressed as:

$$\alpha = 1 - F(h \mid \mathcal{H}_0; M) \Rightarrow h = F^{-1}(1 - \alpha; M) \tag{C.10}$$

$$\beta = 1 - F(h \mid \mathcal{H}_1; \mu_1, M) \Rightarrow M = F^{-1}(1 - \beta; \mu_1, h) \tag{C.11}$$

Hence it is possible to determine a window size that provides a desired probability of detection.